

1 Measurement report: Molecular composition, optical
2 properties, and radiative effects of water-soluble organic
3 carbon in snowpack samples from Northern Xinjiang,
4 China

5
6 Yue Zhou,^{1,2} Christopher P. West,² Anusha P. S. Hettiyadura,² Xiaoying Niu,¹ Hui Wen,¹
7 Jiecan Cui,¹ Tenglong Shi,¹ Wei Pu,¹ Xin Wang,^{1,4*} Alexander Laskin^{2,3*}
8
9

10 ¹ *Key Laboratory for Semi-Arid Climate Change of the Ministry of Education, College*
11 *of Atmospheric Sciences, Lanzhou University, Lanzhou 730000, China*

12 ² *Department of Chemistry,* ³ *Department of Earth Atmospheric and Planetary Sciences,*
13 *Purdue University, West Lafayette, Indiana 47906, United States*

14 ⁴ *Institute of Surface-Earth System Science, Tianjin University, Tianjin 300072, China*
15

16
17 *Correspondence to:* Alexander Laskin (alaskin@purdue.edu) and Xin Wang
18 (wxin@lzu.edu.cn)
19
20
21
22
23
24
25
26
27
28
29

30 **Abstract.** Water-soluble organic carbon (WSOC) in the cryosphere has important
31 impact on the biogeochemistry cycling and snow/ice surface energy balance through
32 changes in the surface albedo. This work reports on chemical characterization of WSOC
33 in 28 representative snowpack samples collected across regional area of northern
34 Xinjiang, northwestern China. We employed multi-modal analytical chemistry
35 techniques to investigate both bulk and molecular-level composition of WSOC and its
36 optical properties, informing the follow-up radiative forcing (*RF*) modeling estimates.
37 Based on the geographic differences and proximity of emission sources, the snowpack
38 collection sites were grouped as urban/industrial (U), rural/remote (R), and soil-
39 influenced (S) sites, for which average WSOC total mass loadings were measured as
40 1968 ± 953 ng g⁻¹ (U), 885 ± 328 ng g⁻¹ (R), and 2082 ± 1438 ng g⁻¹ (S), respectively. The
41 S sites showed the higher mass absorption coefficients at 365 nm (MAC_{365}) of
42 0.94 ± 0.31 m² g⁻¹ compared to those of U and R sites (0.39 ± 0.11 m² g⁻¹ and 0.38 ± 0.12
43 m² g⁻¹, respectively). Bulk composition of WSOC in the snowpack samples and its basic
44 source apportionment was inferred from the Excitation-Emission Matrices and the
45 Parallel Factor analysis featuring relative contributions of two humic-like (HULIS-1
46 and HULIS-2) and one protein-like (PRLIS) components with ratios specific to each of
47 the S, U, and R sites. Additionally, a sample from site 120 showed unique pollutant
48 concentrations and spectroscopic features remarkably different from all other U, R, and
49 S samples. Molecular-level characterization of WSOC using high-resolution mass
50 spectrometry (HRMS) provided further insights into chemical differences among four
51 types of samples (U, R, S, and 120). Specifically, much more reduced S-containing

52 species with high degree of unsaturation and aromaticity were uniquely identified in U
53 samples, suggesting an anthropogenic source. Aliphatic/proteins-like species showed
54 highest contribution in R samples, indicating their biogenic origin. The WSOC
55 components from S samples showed high oxygenation and saturation levels. A few of
56 unique CHON and CHONS compounds with high unsaturation degree and molecular
57 weight were detected in the 120 sample, which might be anthraquinone derivatives from
58 plant debris. Modeling of the WSOC-induced RF values showed warming effects of
59 0.04 to 0.59 $W\ m^{-2}$ among different groups of sites, which contribute up to 16% of that
60 caused by BC, demonstrating the important influences of WSOC on the snow energy
61 budget.
62

63 **1 Introduction**

64 As the largest component of the terrestrial cryosphere (Brutel-Vuilmet et al., 2013),
65 snow covers up to 40% of Earth's land seasonally (Hall et al., 1995). Snowfall is a
66 crucial fresh water, nutrient, and carbon source for land ecosystems (Jones,
67 1999;Mladenov et al., 2012), especially for barren regions such as the northwestern
68 China (Xu et al., 2010). Chemical deposits in the snowpack are highly photochemically
69 and biologically active, which in turn influence biogeochemical cycles and the
70 atmospheric environment (Grannas et al., 2007;Liu et al., 2009). With respect to the
71 climate effects, snow/ice surface has the highest albedo, which makes it the highest
72 light reflecting surface on Earth and a key factor influencing the Earth's radiative
73 balance. The deposition of light-absorbing particles (LAP), primarily black carbon
74 (BC), organic carbon (OC), mineral dust (MD), and microbes, on snow reduces the
75 snow albedo significantly and increases the absorption of solar radiation (Hadley and
76 Kirchstetter, 2012;Skiles et al., 2018). Consequently, deposits of LAP accelerate snow
77 melting (Hansen and Nazarenko, 2004) and affect the snow photochemistry (Zatko et
78 al., 2013), further influencing the regional and global climate (Bond et al., 2013;Flanner
79 et al., 2007;Jacobson, 2004). The albedo reduction and radiative forcing (RF) due to the
80 BC and MD deposits in snow has been a subject of many field studies (Doherty et al.,
81 2010;Huang et al., 2011;Pu et al., 2017;Shi et al., 2020;Wang et al., 2013, 2017b;Zhang
82 et al., 2018b), remote sensing estimates (Painter et al., 2010;Pu et al., 2019), and climate
83 model simulations (He et al., 2014;Qian et al., 2014;Zhao et al., 2014). Darkening of
84 snow by biological organisms, like snow algae common in high-altitude and high-

85 latitude snowpack, has also been investigated (Cook et al., 2017a, b; Ganey et al.,
86 2017; Lutz et al., 2014). However, yet little is known about the chemical compositions,
87 optical properties, and radiative effects of OC compounds in snow, which result from
88 both deposition of organic aerosol from natural and anthropogenic sources as well as
89 deposits of the wind-blown soil organic matter (Pu et al., 2017; Wang et al., 2013).

90 Water-soluble OC (WSOC) contributes to a large portion (10-80%) of organic
91 aerosol (Kirillova et al., 2014; Zhang et al., 2018a) and it is also widely distributed in
92 the cryosphere. The polar ice sheets and mountain glaciers store large amount of organic
93 carbon, which provide approximately $1.04 \pm 0.18 \text{ TgC yr}^{-1}$ of WSOC exported into
94 proglacial aquatic environments (Hood et al., 2015), with a substantial part of it is
95 highly bioavailable (Singer et al., 2012; Zhou et al., 2019c). WSOC components that
96 absorb solar radiation at ultraviolet to visible (UV-Vis) wavelengths are collectively
97 termed as “brown carbon (BrC)” (Andreae and Gelencser, 2006), and have become the
98 subject of many aerosol studies (Laskin et al., 2015). The optical properties of WSOC
99 in snow started to receive attention because its important role in initiating snow
100 photochemistry (McNeill et al., 2012). Anastasio and Robles (2007) first quantified the
101 light absorption of water-soluble chromophores in Arctic and Antarctic snow samples.
102 They found that ~50% of absorption for wavelength greater than 280 nm was attributed
103 to organic chromophores. Subsequently, Beine et al. (2011) determined the light
104 absorption of humic-like substances (HULIS) in snow at Barrow, Alaska. They found
105 that HULIS account for nearly half of the total absorption by dissolved chromophores
106 within the photochemically active wavelength region (300 to 450 nm), concluding that

107 HULIS is a major light absorber in Barrow snow and that the HULIS-mediated
108 photochemistry is probably important for the regional environment. Several recent
109 works have reported the radiative absorption of snow WSOC. Yan et al. (2016)
110 estimated amount of the solar radiation absorbed by WSOC from snow collected in
111 northern Tibetan Plateau (TP), which was 10% relative to that absorbed by BC,
112 indicating a non-negligible role of WSOC in accelerating snow and ice melting. Similar
113 results were also reported for WSOC extracted from other high-mountain areas (Niu et
114 al., 2018; Zhang et al., 2019). However, chemical characterization and optical properties
115 of the light-absorbing WSOC (aka BrC) in cryosphere is still an emerging topic. To date,
116 no field study evaluated yet the composition-specific influence of WSOC on the snow
117 albedo reduction.

118 The fluorescence excitation-emission matrix (EEM) analysis is a sensitive, rapid,
119 and non-destructive optical spectroscopy method (Birdwell and Valsaraj, 2010) that has
120 been used to investigate the bulk composition and attribute potential sources of
121 chromophoric WSOC in aquatic ecosystems (Jaffé et al., 2014) and more recently in
122 aerosols (Chen et al., 2016b, 2020; Fu et al., 2015; Mladenov et al., 2011; Wu et al.,
123 2019b). Based on parallel factor (PARAFAC) analysis, contributions from main
124 fluorescent components such as different fractions of HULIS and protein-like
125 substances (PRLIS) can be quantitatively evaluated (Stedmon and Bro, 2008),
126 indicating plausible sources of WSOC in aquatic (Murphy et al., 2008) and atmospheric
127 samples (Wu et al., 2021). The chemical interpretations of PARAFAC-derived
128 components are relatively well characterized for aquatic WSOC, but it may not be

129 simply applied to WSOC in snow because their sources and geochemical processes are
130 highly different (Wu et al., 2021).

131 High resolution mass spectrometry (HRMS) interfaced with soft electrospray
132 ionization (ESI) can help to decipher complexity of WSOC, providing explicit
133 description of its individual molecular components (Qi et al., 2020). Thousands of
134 individual organic species with unambiguously identified elemental composition can
135 be detected at once by ESI-HRMS due to its high mass resolving power, mass accuracy,
136 and dynamic range (Nizkorodov et al., 2011;Noziere et al., 2015). Combined with a
137 high-performance liquid chromatography (HPLC) separation stage and photodiode
138 array (PDA) detector, the integrated HPLC-PDA-HRMS platform enables separation
139 of WSOC components into fractions with characteristic retention times, UV–vis spectra,
140 and elemental composition. Correlative analysis of these multi-modal data sets
141 facilitates comprehensive characterization of chromophores present in complex
142 environmental mixtures (Laskin et al., 2015;Lin et al., 2016, 2018;Wang et al., 2020a).
143 Presently, HRMS studies of WSOC exist in the cryosphere are still limited to the
144 snow/ice in polar regions (Antony et al., 2014, 2017;Bhatia et al., 2010) and mountain
145 glaciers in the Alps (Singer et al., 2012) and on the TP (Feng et al., 2016;Spencer et al.,
146 2014;Zhou et al., 2019a) that with perennial snowpack. For the regions mentioned
147 above, WSOC in snow/ice samples is dominated by proteins- or lipids-like compounds
148 from autochthonous microbial activity with high bioavailability. Whereas, snow in
149 northwestern China is seasonal, the snowpack persists for 3-6 months annually, and its
150 composition is substantially influenced by local soil dust and deposited aerosols from

151 both natural and anthropogenic sources (Pu et al., 2017). Therefore, the chemical
152 compositions and optical properties of WSOC from this area snowpack is likely
153 different from those reported for the remote regions with more persistent snow coverage.

154 In this study, seasonal snow samples were collected across the northern Xinjiang
155 region of China, in January 2018. We investigate the optical and molecular
156 characteristics of WSOC using a range of analytical techniques, including UV-Vis
157 absorption spectrophotometry, EEM, and HPLC-ESI-HRMS. Furthermore, based on
158 the measured optical properties and concentrations of snow impurities, as well as the
159 physical properties of snow at each site, we calculate for the first time extent of RF
160 attributed to WSOC in snow.

161

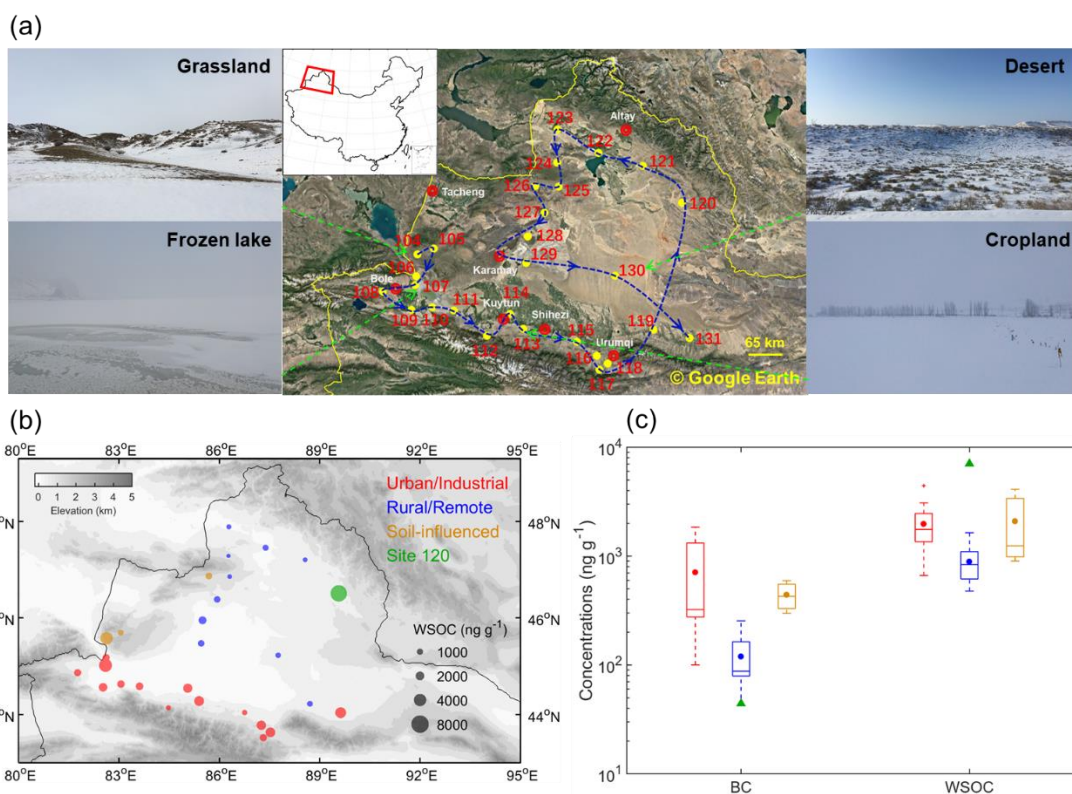
162 **2 Methods**

163 **2.1 Sample collection**

164 28 surface and 8 subsurface snow samples were collected from 28 sites in Xinjiang,
165 northwestern China during a road trip in January 2018. The area map and sampling
166 locations are shown in Fig. 1a. The sampling sites were numbered in chronological
167 order and with numbering scheme adopted from our previous campaigns (Pu et al.,
168 2017; Wang et al., 2013, 2017b; Ye et al., 2012). The sampling sites were classified into
169 four groups based on their geographical location and proximity to urban areas (Table
170 S1): urban/industrial (U) sites (no. 106-118, and 131), rural/remote (R) sites (no. 119,
171 121-125, and 127-130), soil-influenced (S) sites (no.104, 105, and 126), and site 120.
172 The U sites were located north of Tianshan Mountains, near major cities in Xinjiang

173 area. These sites were more likely influenced by local anthropogenic emissions (Pu et
174 al., 2017). The rest of the sites were assigned to R group, most of them were from desert
175 area or barren grasslands located at least ~50-100 km from major cities; hence, they
176 were mostly influenced by natural sources. The S sites are a subgroup of the R group,
177 they correspond to specific locations where the snowpack was visibly patchy and
178 shallow, so local soil could be blown into snow by strong winds. For the S samples, the
179 coarse mineral particles of yellow/brown color were clearly seen on the filters following
180 snow water filtration (Fig. S1), consistent with the expected high loadings of soils at
181 these sites. Out of R group, a sample from site 120 was considered separately because
182 it showed composition and optical characteristics inconsistent with all other samples.
183 For instance, it had very low BC concentration but highest WSOC concentration among
184 all the samples; hence, it is discussed separately.

185



186

187 **Figure 1.** (a) Sampling locations and site numbers with photographs for typical land use types of
 188 sampling sites. (b) Spatial distribution of WSOC concentrations in snow. Sampling sites are divided
 189 into four groups indicated by different colors. The bubble sizes are proportional to the WSOC
 190 concentrations. (d) Variations of BC and WSOC concentrations among four groups of sites. The
 191 boxes denote the 25th and 75th quantiles, and the horizontal lines represent the medians, the
 192 averages are shown as dots; the whiskers denote the maximum and minimum data within 1.5 times
 193 the interquartile range, and the data points out of this range are marked with crosses (+).

194

195 Details of the sampling procedures can be found elsewhere (Wang et al., 2013) and
 196 they are briefly described here. The snow sampling sites were selected at least 20 km
 197 from cities and villages and at least 1 km upwind of the approach road or railway, such
 198 that the influence from single-point very local sources were minimized and the samples

199 would rather reflect conditions of large regional areas. The snow samples were
200 collected in sterile plastic bags (Whirl-Pak, Nasco, WI, USA) using clean, stainless
201 steel utensils and by scooping ~ 3 L of snow on top 5 cm at each site, resulting in ~600
202 mL volume of melted snow water. For several sites with snowpack deeper than 10 cm,
203 subsurface snow (~5-10 cm) was also collected. Snow depths, snow density, and snow
204 temperature were also measured for each sampled snow layer (Shi et al., 2020). All
205 collected samples were then stored in a freezer (< -20 °C) until further processing. 28
206 surface samples were analyzed by the following analytical techniques.

207

208 **2.2 Chemical species analysis**

209 The snow samples were melted under room temperature and immediately filtered
210 by Polytetrafluoroethylene (PTFE) syringe filters with pore size of 0.22 µm (Thermo
211 Fisher, Inc.) to remove insoluble solids. Obtained filtrates were then used for the
212 measurements of concentrations of soluble inorganic ions, mass loadings of WSOC,
213 acquisition of bulk UV-Vis absorption and EEM spectra, and molecular characterization
214 using HPLC-ESI-HRMS platform.

215 The major inorganic ions (Na^+ , NH_4^+ , K^+ , Mg^{2+} , Ca^{2+} , Cl^- , SO_4^{2-} , and NO_3^-)
216 were measured by an ion chromatography system (Dionex 600, Thermo Scientific, MA,
217 USA) using an IonPac AS22 column for anions and an IonPac CS12A column for
218 cations. The detection limits for all inorganic ions are greater than 0.05 mg L⁻¹. The
219 concentrations of WSOC were analyzed by a total organic carbon analyzer (Aurora
220 1030W, OI Analytical, TX, USA). Each measurement was done in triplicate, the

221 average concentrations of four groups of samples and the values for each sample after
222 blank subtraction are presented in Tables S2 and S3, respectively. The detection limit
223 and relative standard deviation of measurements were 2 ppb and 1%, respectively.

224 The BC concentrations in snow were measured by a custom-developed two-sphere
225 integration (TSI) spectrophotometer (Wang et al., 2020b), and have been reported by
226 Shi et al. (2020). The distribution of BC concentrations in snow samples is also shown
227 in Fig. S2.

228

229 **2.3 UV-Vis absorption and fluorescence EEM spectroscopic measurements**

230 The UV-Vis absorption and fluorescence EEM spectra were recorded
231 simultaneously by an Aqualog spectrofluorometer (Horiba Scientific, NJ, USA) in a 1
232 cm quartz cuvette. The excitation wavelengths for EEM were 240 to 600 nm in intervals
233 of 5 nm and were the same for UV-Vis spectrum acquisition. The fluorescence emission
234 range was 250 to 825 nm in 5 nm intervals with an integration time of 0.5 s. An ultrapure
235 water (18.2 MΩ cm, Milli-Q purification system, Millipore, Bedford, MA, USA) was
236 used for blank measurement, subtracted from all sample spectra.

237 The absorbance at 600 nm was subtracted from the whole spectrum to correct the
238 scattering effects and baseline shifts of the instrument (Chen et al., 2019). The BrC
239 mass absorption coefficients (MAC ; $m^2 g^{-1}$) related to WSOC contributions were
240 calculated by:

$$241 \quad MAC_{BrC}(\lambda) = \frac{\ln(10) \cdot A(\lambda)}{C_{WSOC} \cdot L} \quad (1)$$

242 Where λ is the wavelength, A is the base-10 absorbance measured by the

243 spectrophotometer, C_{WSOC} (mg L^{-1}) is the concentration of WSOC, L is the cuvette path
244 length (0.01 m). To characterize the wavelength dependence of MAC_{B+C} , absorption
245 Ångström exponents (AAE) were determined by a power-law regression (Kirchstetter
246 et al., 2004):

$$247 \quad MAC(\lambda) = k \cdot \lambda^{-AAE}, \quad (2)$$

248 where k is a constant related to WSOC concentrations. To exclude absorption due to
249 inorganic chromophores (e.g., nitrate), the AAE values were derived from the power
250 law fits limited to the range of 330- 400 nm ($AAE_{330-400}$) (Yan et al., 2016).

251 Processing of the EEM data followed the protocols described elsewhere (Zhou et
252 al., 2019b). Briefly, the raw EEM data sets were first background subtracted to remove
253 the water Raman scatter peaks, then the inner filter effect was corrected (Kothawala et
254 al., 2013). The fluorescence intensities were normalized to water Raman unit (RU)
255 (Lawaetz and Stedmon, 2009). The processed EEM data was analyzed by the
256 PARAFAC model in the manner similar to our previous report (Zhou et al., 2019b). In
257 this study, the PARAFAC modeling was conducted using drEEM toolbox (version 0.2.0,
258 <http://models.life.ku.dk/drEEM>) (Murphy et al., 2013). According to the analysis of
259 residual errors of 2- to 7- component models and split half analysis, a 3-component
260 model was selected. Only 2- and 3-component models have passed the split-half
261 analysis with the “S4C6T3” split scheme (Fig. S3) (Murphy et al., 2013). Moreover,
262 the sum of residual error decreased significantly when the number of components
263 increased from 2 to 3 (Fig. S4). The spectra of derived fluorescent components appeared
264 consistent with those commonly found in other studies (Table S4).

265 **2.4 HPLC-ESI-HRMS Molecular Analysis and data processing**

266 The WSOC extracts were desalted and concentrated through solid phase extraction
267 (SPE) method using DSC18 cartridges (Supelco, Millipore Sigma, PA, USA). The
268 cartridges were conditioned and equilibrated by one-column volume (~3 mL) of
269 acetonitrile (ACN, Optima, LC-MS grade, Fisher Scientific Inc.) and one-column
270 volume of water (Optima, LC-MS grade, Fisher Scientific Inc.), respectively. To
271 increase the efficiency of SPE, the sample was acidified to pH \approx 2 using HCl (Lin et al.,
272 2010), and 3 mL of acidified sample flowed through the cartridge at a low flow rate of
273 1-2 drops per second. Salts and other unretained compounds (e.g., small molecular
274 acids and carbohydrates) were first washed out by one-column volume of water, and
275 the analyte retained on the cartridge was then eluted by two-column volumes of ACN.
276 The efficiency of SPE was evaluated by measuring the UV-Vis absorption before and
277 after elution and ensured the good recovery of analytes (Text S1). The ACN eluents
278 were concentrated to 150 μ L under a gentle stream of pure N₂, and then diluted by
279 adding 150 μ L of ultrapure water. Finally, the reconstituted extracts were further
280 concentrated to 200 μ L prior to HPLC analysis.

281 The obtained extracts were analyzed using a Vanquish HPLC system coupled to a
282 Q Exactive HF-X Orbitrap HRMS with an IonMAX ESI source (all from Thermo
283 Scientific Inc.). The HPLC separation was performed on a Phenomenex Luna C18
284 revised-phase column (2 mm \times 150 mm, 5 μ m particles, 100 Å pores). A gradient
285 elution was performed at a flow rate of 200 μ L/min by an A + B binary mobile phase
286 system: (A) water with 0.05% v/v formic acid and (B) acetonitrile with 0.05% v/v

287 formic acid (Optima, LC-MS grade, Fisher Scientific Inc.). The elution protocol was
288 0–3 min hold at 90% A, 3–90 min linear gradient to 0% A, 90–100 min hold at 0% A,
289 and then 100–130 min hold at 90% A to recondition the column for the next sample.
290 The column temperature was maintained at 25 °C and the sample injection volume was
291 25 µL. The UV-vis absorption of eluted chromophores was recorded by a PDA detector
292 over the wavelength range of 200 to 680 nm. Correlation analysis between PDA and
293 MS peaks and relative absorption of different chromophore fractions will be discussed
294 in an upcoming paper. For ESI-HRMS analysis, the following settings were used: 45
295 units of sheath gas, 10 units of auxiliary gas, 2 units of sweep gas, a spray voltage of
296 3.5 kV, a capillary temperature of 250 °C, and a sweep cone was used. The mass spectra
297 were acquired at a mass range of 80–1,200 Da at mass resolving power of $\Delta m/m =$
298 240,000 at m/z 200. Mass calibration was performed using commercial calibration
299 solutions (PI-88323 and PI-88324, Thermo Scientific) for ESI(+/-) modes.

300 The raw experimental data files were acquired by Xcalibur software (Thermo
301 Scientific Inc.). The HPLC-ESI-HRMS data sets were preliminary processed using an
302 open source software toolbox, MZmine 2 (<http://mzmine.github.io/>), to perform peak
303 deconvolution and chromatogram construction (Myers et al., 2017; Pluskal et al., 2010).
304 The background subtraction and formula assignment were performed using customized
305 Microsoft Excel macros (Roach et al., 2011). The formulas were assigned based on
306 first- and second-order Kendrick mass defects and a MIDAS formula calculator
307 (<http://magnet.fsu.edu/~midas/>). $[M + H]^+$, $[M + Na]^+$, and $[M - H]^-$ ions were assumed
308 to identify products detected in ESI+ and ESI- modes, respectively. Besides, adduct

309 ions were also identified and removed using a homemade MATLAB script (Text S2).
310 The molecular formulas were assigned using the following constraints: $1 \leq C \leq 50$, $1 \leq$
311 $H \leq 100$, $N \leq 5$, $O \leq 50$, $S \leq 1$, and $Na \leq 1$ (ESI+ only) and mass tolerance of <3.0 ppm.
312 Furthermore, to eliminate the formulas not likely to be observed in nature, the elemental
313 ratio limits of $0.3 \leq H/C \leq 3.0$, $0.0 \leq O/C \leq 3.0$, $0.0 \leq N/C \leq 1.3$, $0.0 \leq S/C \leq 0.8$ (Lin
314 et al., 2012; Wang et al., 2018) were applied. The double-bond equivalent (DBE) values
315 of the neutral assigned species $C_cH_hO_oN_nS_s$ were calculated using the equation:

$$316 \quad DBE = c - \frac{h}{2} + \frac{n}{2} + 1 \quad (3)$$

317 The aromaticity index (AI) is a conservative criterion for the unequivocal identification
318 of aromatic and condensed aromatic structures in natural organic matter calculated as
319 (Koch and Dittmar, 2006, 2016):

$$320 \quad AI = \frac{1 + c - o - s - 0.5(h+n)}{c - o - n - s}, \quad (4)$$

321 $AI > 0.5$ and $AI \geq 0.67$ are unambiguous minimum thresholds for the presence of
322 aromatic and condensed aromatic structures in a molecule, respectively. If either the
323 numerator or denominator in Eq. (4) equals to 0, then AI is assigned with 0 value.

324 The intensity (I^*) weighted molecular weight (MW_w) and other characteristic
325 molecular parameters of H/C (H/C_w), O/C (O/C_w), DBE (DBE_w), DBE/C (DBE/C_w), and
326 AI (AI_w) were calculated using Eq. (5):

$$327 \quad X_w = \frac{\sum(I_i^* \cdot X_i)}{\sum I_i^*}, \quad (5)$$

328 where X_w represents any of the weighted parameters introduced above; I_i^* , and X_i are
329 the corresponding intensity and the molecular parameter values calculated for each
330 assigned species i , respectively.

331 **2.5 Snow Albedo Modeling and Radiative Forcing Calculations**

332 The spectral snow albedo was calculated by the Snow, Ice, and Aerosol Radiative
333 (SNICAR) model (Flanner et al., 2007), which accounts for the radiative transfer in the
334 snowpack based on the theory from Wiscombe and Warren (1980) and the two-stream,
335 multilayer radiative approximation (Toon et al., 1989). The input parameters required
336 for the SNICAR model are snow depth, snow density, effective snow grain size, solar
337 zenith angle, and impurity concentrations. Snow depth and density were measured in
338 the field. The effective snow grain size was retrieved from the spectral albedo measured
339 in the field, and detailed information can be found in our previous study (Shi et al.,
340 2020). The solar zenith angle was calculated using the site location and sampling date
341 for each site. The input values of parameters for the SNICAR model, which are those
342 for surface snow, are summarized in Table S5. For simplicity, a homogenous snowpack
343 assumption was applied for both snow physical properties and pollutants concentrations.

344 To evaluate influence of BrC attributed to WSOC on the snow albedo, optical
345 properties of BrC material such as single scattering albedo (*SSA*), asymmetry factor (*g*),
346 and mass extinction coefficient (*MEC*) are needed as inputs for simulation. These
347 parameters were calculated by Mie theory, approximating WSOC as an ensemble of
348 small BrC particles distributed evenly in the snowpack. The input variables required
349 for Mie calculation are complex refractive index ($RI = n - ik$) and particle size parameter
350 ($x = \pi d/\lambda$). The diameter of individual particles (*d*), density (ρ), and the real part (*n*) of
351 *RI* of WSOC were assumed to be 150 nm, 1.2 g cm⁻³, and 1.55 (constant in the UV-Vis
352 range), respectively (Chen and Bond, 2010; Lu et al., 2015b). The imaginary part (*k*) of

353 RI was calculated as (Sun et al., 2007):

$$354 \quad k(\lambda) = \frac{MAC \cdot \rho \cdot \lambda}{4\pi}. \quad (6)$$

355 Then, SSA , g , and extinction cross-section (Q_{ext}) were derived from Mie code
356 (<https://omlc.org/software/mie/>), and the obtained values were then used to calculate
357 MEC as (Seinfeld and Pandis, 2016):

$$358 \quad MEC = \frac{\pi d^2 / 4 \cdot Q_{ext}}{\pi d^3 / 6 \cdot \rho}. \quad (7)$$

359 The spectral albedo (α_λ) was calculated for the scenarios of pure snow and BC/BrC-
360 contaminated snow. After that, the broadband albedo (α) of each scenario needs to be
361 determined to calculate the broadband albedo reduction ($\Delta\alpha$) and RF due to different
362 types of impurities. α was derived by integration of α_λ over the wavelength range of 300
363 to 1500 nm weighted by the incoming solar irradiance $S(\lambda)$.

$$364 \quad \alpha = \frac{\int_{300}^{1500} \alpha_\lambda S(\lambda) d\lambda}{\int_{300}^{1500} S(\lambda) d\lambda}. \quad (8).$$

365 The incoming solar irradiance were simulated by Coupled Ocean-Atmosphere
366 Radiative Transfer (COART) model (<https://cloudsgate2.larc.nasa.gov/jin/coart.html>)
367 (Jin et al., 2006) for each site under clear sky assumption, therefore the calculated RF
368 can be considered as upper limits.

369 The RF resulted from either BC or BrC in snow ($RF_{BC,BrC}$) were calculated by
370 multiplying the downward shortwave solar radiation flux at surface by $\Delta\alpha_{BC,BrC}$ (Painter
371 et al., 2013):

$$372 \quad RF_{BC,BrC} = E \cdot \Delta\alpha_{BC,BrC}, \quad (9)$$

$$373 \quad \Delta\alpha_{BC,BrC} = (\alpha_{pure\ snow} - \alpha_{BC,BrC}), \quad (10)$$

374 where E is the average-daily downward shortwave solar radiation flux acquired from

375 NASA's Clouds and the Earth's Radiant Energy System (CERES) product "CERES
376 SYN1deg" (<https://ceres.larc.nasa.gov/products.php?product=SYN1deg>). $\alpha_{pure\ snow}$ and
377 $\alpha_{BC,BrC}$ are the broadband albedo of pure snow and BC or BrC contaminated snow,
378 respectively.

379

380 **3 Results and Discussions**

381 **3.1 Characteristics of chemical species**

382 Figure 1b shows mass concentrations of WSOC measured in the snow samples,
383 illustrating their broad range from 478 to 7069 ng g⁻¹ with an average of 1775±1424 ng
384 g⁻¹ (arithmetic mean ± 1 standard deviation, and same below). The U and the S sites
385 showed higher concentrations with averages of 1968±953 ng g⁻¹ and 2082±1438 ng g⁻¹,
386 respectively, while the value of R sites (885±328 ng g⁻¹) was approximately a factor
387 of two lower (Table S2). Of note, the WSOC concentrations in U and S samples
388 reported here are significantly higher than those found in the snow and ice from polar
389 regions (~40 – 500 ng g⁻¹) (Fellman et al., 2015;Hagler et al., 2007a, b;Hood et al.,
390 2015), glaciers on the European Alps (~100 – 300 ng g⁻¹) (Legrand et al., 2013;Singer
391 et al., 2012), and the remote TP region (~150 – 700 ng g⁻¹) (Yan et al., 2016). However,
392 our reported WSOC mass concentrations are in the same range as those in the fresh
393 snow samples collected from Laohugou (LHG) glacier, northern TP (2000 – 2610 ng g⁻¹)
394 (Feng et al., 2018). It has been reported that glaciers and ice sheets from polar or
395 alpine regions store a large amount of WSOC and discharge it to their downstream
396 terrestrial ecosystems (Hood et al., 2009, 2015;Singer et al., 2012). Comparable or even

397 higher concentrations of WSOC in our samples indicate that the seasonal snow in
398 Northern Xinjiang is also an important organic carbon source for the terrestrial
399 ecosystems during spring meltdown.

400 As shown in Fig. 1c, the U sites were also associated with the highest BC
401 concentrations among all four groups (mean: $707 \pm 651 \text{ ng g}^{-1}$). Furthermore, the mass
402 contributions of sulfate ions at U sites (Table S2, mean: $33\% \pm 7\%$), which is a
403 commonly-used marker for fossil fuel burning (Pu et al., 2017), were approximately
404 twice as high as those from the other sites. All these results indicate strong influence
405 from anthropogenic pollution sources, explaining high WSOC loadings at U sites. For
406 the S sites, HULIS from local soil may dominate the WSOC composition. For example,
407 snow at site 104 was patchy and thin (Fig. 1a, grassland), the local black soil can be
408 lifted by winds and then redeposited and mixed with snow. The assumption of soil
409 contributions agrees with observed high mass contribution of calcium ions in S samples
410 (mean: $50\% \pm 4\%$, see Table S2). Although WSOC concentrations in R samples were
411 relatively low ($885 \pm 328 \text{ ng g}^{-1}$), they were still higher than most of the values from
412 high-altitude or high-latitude regions of previous studies ($\sim 40 - 700 \text{ ng g}^{-1}$ as mentioned
413 in the last paragraph). It might be explained by two reasons: (1) more intensive
414 anthropogenic emissions in the northern Xinjiang region; (2) there was little snowfall
415 during 2018 campaign; therefore, WSOC had been potentially accumulated on the snow
416 surface by sublimation and dry deposition (Doherty et al., 2010). The sample from site
417 120 is discussed separately as it exhibited the highest WSOC concentration (7069 ng g^{-1})
418 and almost the lowest BC concentration (44 ng g^{-1}) out of all samples analyzed in

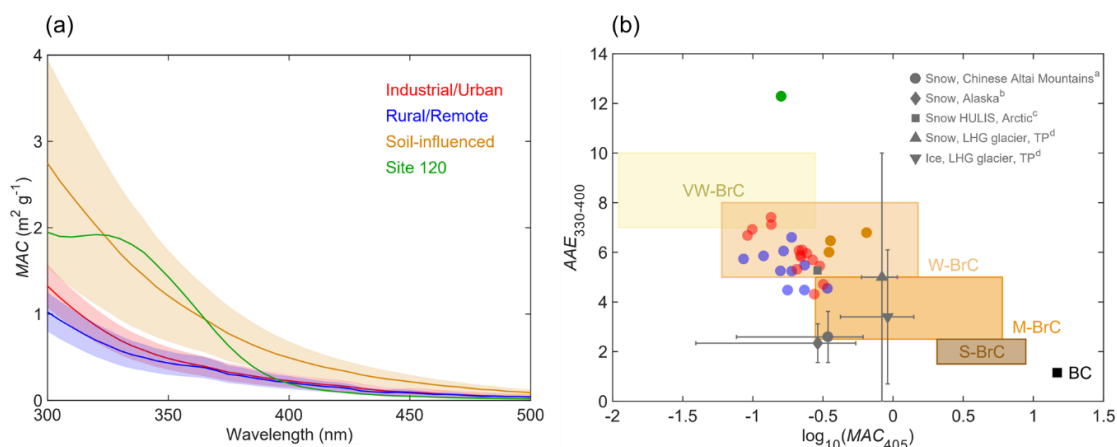
419 this work. The potential sources of WSOC from site 120 sample will be discussed in
420 section 3.3.

421

422 **3.2 Bulk light-absorbing and fluorescence properties**

423 The average MAC_{BrC} spectra of WSOC from different groups of samples are shown
424 in Fig. 2a. The average MAC_{BrC} at 365 nm (MAC_{365}) of S samples ($0.94\pm 0.31 \text{ m}^2 \text{ g}^{-1}$)
425 was significantly higher than those of U ($0.39\pm 0.11 \text{ m}^2 \text{ g}^{-1}$) and R ($0.38\pm 0.12 \text{ m}^2 \text{ g}^{-1}$)
426 samples, respectively (Table S2). The information on MAC_{BrC} related to WSOC in snow
427 and ice is yet very scarce in literature. The MAC_{365} values of U and R samples are
428 comparable with the results reported for continental snow collected across Alaska
429 ($0.37\pm 0.32 \text{ m}^2 \text{ g}^{-1}$) (Zhang et al., 2020), but slightly lower than those of snow WSOC
430 from Chinese Altai Mountains, which shows a wide range from $\sim 0.3 \text{ m}^2 \text{ g}^{-1}$ for
431 accumulation season to $\sim 1.0 \text{ m}^2 \text{ g}^{-1}$ for ablation season with an average of 0.45 ± 0.35
432 $\text{m}^2 \text{ g}^{-1}$ (Zhang et al., 2019), and HULIS extracted from Arctic snow ($\sim 0.5 \text{ m}^2 \text{ g}^{-1}$) (Voisin
433 et al., 2012). The snow/ice samples from LHG glacier on the TP (Yan et al., 2016)
434 presented a higher average MAC_{365} ($1.3 - 1.4 \text{ m}^2 \text{ g}^{-1}$) than the S samples; they also
435 indicated large contribution of dust-derived organics. The relative lower values of
436 MAC_{365} measured for U samples might be explained by photobleaching of WSOC
437 during aging on the snow surface (Yan et al., 2016; Zhang et al., 2019). Due to the
438 stronger wavelength dependence of WSOC from U samples ($A_{AE330-400}$: 6.0 ± 0.8 vs.
439 5.4 ± 0.7 for U and R sites, respectively), their MAC values at shorter wavelength of 300
440 nm were higher compared to those of R samples. For example, the averages of MAC_{300}

441 were $1.32 \pm 0.24 \text{ m}^2 \text{ g}^{-1}$ and $1.02 \pm 0.21 \text{ m}^2 \text{ g}^{-1}$ for U and R samples, respectively (Table
 442 S2). The $AAE_{330-400}$ of our samples were in the range of 4.3 to 12.3 (mean: 6.0 ± 1.5),
 443 and S sites had a higher average of 6.4 ± 0.3 than those corresponding to U and R samples.
 444 The highest $AAE_{330-400} = 12.3$ was found for WSOC from site 120 sample, and its UV-
 445 Vis spectrum also exhibited an unusual spectral shape with a well-defined spectral
 446 feature observed between 300 and 350 nm. Similar feature was reported in: (1)
 447 cryoconite samples collected from TP glaciers (Feng et al., 2016), which may be
 448 attributed to mycosporine-like amino acids (MAAs) produced by microorganisms (e.g.
 449 fungi, bacteria, and algae) (Elliott et al., 2015; Shick and Dunlap, 2002); (2) Plant-
 450 derived (e.g., corn, hairy vetch, or alfalfa) water extractable organic matter containing
 451 phenolic carboxylic compounds (He et al., 2009).



452
 453 **Figure 2.** (a) The average MAC spectrum of BrC attributed to WSOC in each group (solid lines,
 454 denoted by different colors), the shaded areas represent one-time standard deviations. (b) Plot of the
 455 optical-based BrC classification scheme (Saleh, 2020) in the $\log_{10}(MAC_{405}) - AAE_{330-400}$ space. The
 456 shaded areas represent very weakly absorbing BrC (VW-BrC), weakly absorbing BrC (W-BrC),
 457 moderately absorbing BrC (M-BrC), and strongly absorbing BrC (S-BrC). BC is also shown for
 458 reference (Bond and Bergstrom, 2006). Grey marks indicate the data from literatures for snow/ice

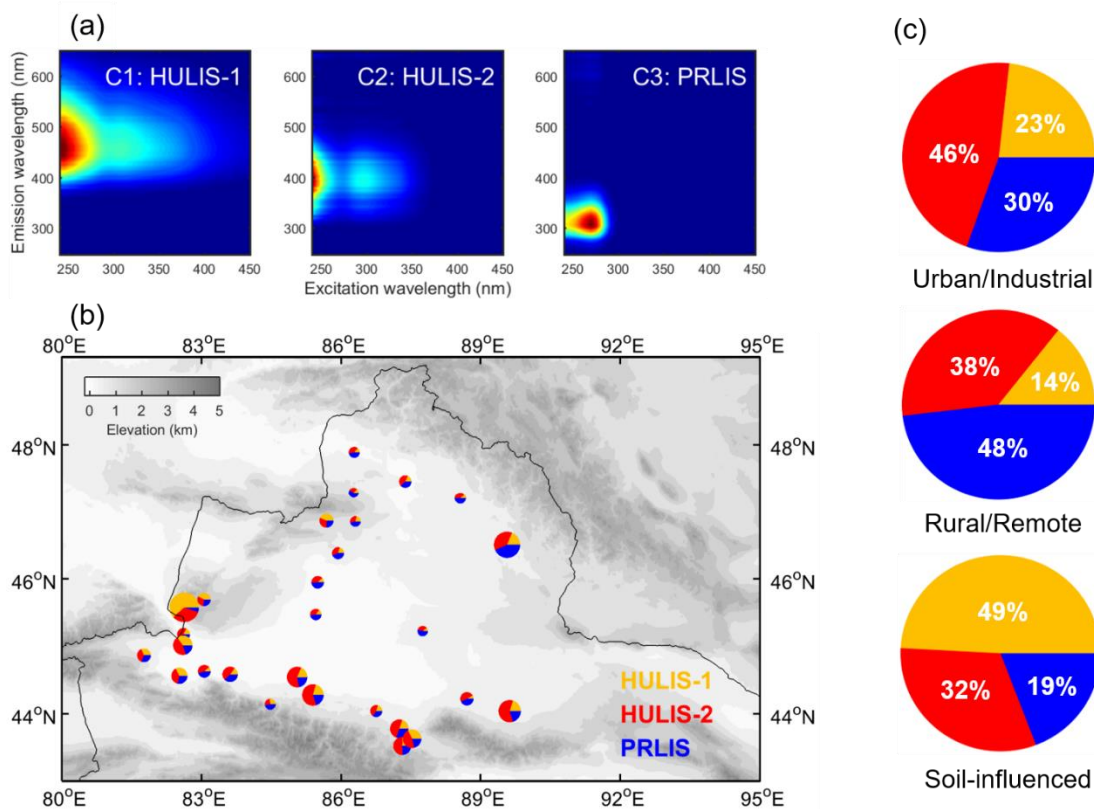
459 samples from Chinese Altai Mountains (^a Zhang et al., 2019), Alaska (^b Zhang et al., 2020), Arctic
460 (^c Voisin et al., 2012, *AAE* is calculated for 300-400 nm), LHG glacier on the TP (^d Yan et al., 2016).
461 Error bars denote the standard deviations of *AAE* or *MAC* values.

462

463 Figure 2b shows *MAC* and *AAE*₃₃₀₋₄₀₀ values measured for BrC attributed to WSOC
464 from our samples in the context of an optical-based classification of BrC presented
465 recently by Saleh (2020). The optical properties characterizing the BrC classes are
466 expected to be associated with their corresponding physicochemical properties (i.e.,
467 molecular sizes, volatility, and solubility). Most of our samples and HULIS in Arctic
468 snow (Voisin et al., 2012) fall into the region of weakly absorbing BrC (W-BrC). The
469 WSOC in snow/ice from Alaska, Chinese Altai Mountains, and LHG glaciers were
470 assigned to moderately absorbing BrC (M-BrC) but with broader ranges, likely
471 indicating higher molecular variability. These results provide a useful dataset of snow
472 BrC light-absorbing properties which may inform climate models.

473 Three fluorescent components (i.e., C1, C2, and C3) were identified by PARAFAC
474 analysis (Fig. 3a). The peak positions of each component are summarized in Table S4.
475 C1 (HULIS-1) is a type of terrestrial-derived humic fluorophore with long emission
476 wavelengths, commonly reported for samples of terrestrial aquatic systems and highly-
477 oxygenated organic aerosols (Chen et al., 2016a; Stedmon et al., 2003). C2 (HULIS-2)
478 is usually recognized as HULIS from marine sources (Coble, 1996) or phytoplankton
479 degradation in fresh water (Zhang et al., 2010), and it was also detected in
480 anthropogenic wastewater (Stedmon and Markager, 2005) or industrial-sourced aerosol

481 (Chen et al., 2020). C3 is a class of PRLIS (tyrosine-like) widely found in terrestrial
 482 organics (Wu et al., 2020;Zhang et al., 2010;Zhao et al., 2016) related to labile organic
 483 matter produced from microbial processes (Coble et al., 1998). Of note, the
 484 fluorophores detected in our samples show the similar peak positions compared to the
 485 previous reports for aerosol or aquatic environments, but they do not necessarily have
 486 the same sources due to large differences of the physicochemical and geochemical
 487 processes (Chen et al., 2016b;Duarte et al., 2007).



488 **Figure 3.** (a) The fingerprints of three fluorescent components identified by PARAFAC analysis. (b)
 489 Relative contributions of three components to total fluorescence at each site. HULIS-1, HULIS-2,
 490 and PRLIS are represented in yellow, red, and blue, respectively. The size of each pie is proportional
 491 to the total fluorescence intensity at each site. (c) The average contributions of three components in
 492 different groups of samples.
 493

494 As shown in Figs. 3b and 3c, the relative intensities of three fluorescent
495 components were highly variable among different groups of samples, suggesting
496 systematic substantial differences in their chemical compositions. HULIS-1 dominates
497 in the S samples, where it accounts for ~49% of the total fluorescence (Table S2). In
498 addition, the relative intensities of HULIS-1 are positively correlated with the mass
499 fractions of calcium ion ($r=0.73$, $p<0.01$, Table S6). These results suggest terrestrial
500 origin (soil dust) of HULIS-1, which is consistent with previous studies of water
501 systems and aerosols (Chen et al., 2016a, 2020; Stedmon et al., 2003). A strongly
502 negative correlation between the contributions of HULIS-1 and nitrate mass fractions
503 is found as well ($r=-0.68$, $p<0.01$), reflecting the potential important role of HULIS in
504 snow nitrate photochemistry (Handley et al., 2007; Yang et al., 2018). For instance,
505 Yang et al. (2018) found that HONO formation is significantly enhanced, in the
506 presence of humic acid, from nitrate photolysis. HULIS-2 dominates U samples with
507 an average contribution of ~46%. Given the significantly positive correlation between
508 the contributions of HULIS-2 and mass fractions of sulfate ion ($r=0.51$, $p<0.01$), the
509 primary relevance of anthropogenic emissions for HULIS-2 is confirmed. The R
510 samples show significant contribution of PRLIS fluorophore (mean: $48\% \pm 6\%$),
511 indicating an important role of microbial processes in the composition of WSOC in
512 these samples. This observation is in line with previous studies showing that snow is
513 not only an active photochemical site, but also a biogeochemical reactor in the nitrogen
514 cycling (Amoroso et al., 2010). Amoroso et al. (2010) found that nitrate and nitrite ions
515 in snow collected from Ny-Ålesund, Norway, were most likely from microbial

516 oxidation of ammonium ions. Therefore, the significant correlation ($r=0.78$, $p<0.01$)
517 between relative intensities of PRILS and nitrate mass fractions might be interpreted
518 by: (1) low anthropogenic emissions and local soil dust import (Less contributions of
519 sulfate and calcium ions) and (2) potential metabolic production of nitrate/nitrite in
520 snow at R sites. Further research is needed to investigate this hypothesis in more detail.
521 Of interest, EEM from site 120 sample cannot be modeled well by PARAFAC (Fig. S5)
522 because of the uncommon spectroscopic feature with emission and excitation
523 wavelengths of 315 nm and 452 nm, respectively. This feature is possibly attributed to:
524 (1) NADH (Nicotinamide adenine dinucleotide) -like compounds, which is an indicator
525 for the metabolism of organisms (Pöhlker et al., 2012) or (2) plant-derived water
526 extractable organic matter (Hunt and Ohno, 2007), e.g., corn. This result suggests strong
527 influence from either microbial activity or plant-sourced organics in snow at site 120,
528 which is also consistent with the UV-Vis spectrum shape.

529

530 **3.3 Molecular-level insights into composition of WSOC from snow samples**

531 **3.3.1 General HRMS characteristics**

532 Numbers of assigned species ranged from 561 to 1487 and from 339 to 1568 for
533 ESI+ and ESI- modes, respectively, suggesting high variations of molecular
534 components of WSOC in the snow samples from northern Xinjiang. The assigned peaks
535 accounted for majority (49% – 68%) of all detected MS peaks. Due to the different
536 ionization mechanisms between positive and negative ESI (Lin et al., 2012), only small
537 amounts of compounds were detected in both modes, accounting for approximately 15%

538 of total assignments at each representative site (Fig. S6). The assigned formulas were
539 classified into eight categories, i.e., CHO, CHON, CHOS, CHONS, CH, CHS, CHN,
540 CHS. CHONS referred to formulas containing carbon, hydrogen, oxygen, nitrogen and
541 sulfur elements, and other categories were defined analogously. The U samples had the
542 highest number of assigned compounds among four groups of sites in both ESI+ and
543 ESI- with averages of 1113 ± 203 and 871 ± 287 , respectively (Tables 1 and 2), whereas
544 the number of assigned species from S samples were lowest (mean: 727 ± 146 and
545 438 ± 84 for ESI+ and ESI- modes, respectively), reflecting high molecular complexity
546 of U samples. The numbers of assigned formulas in this study are comparable with the
547 assignments reported for urban aerosol samples (~ 800 – 1800) (Lin et al., 2012; Wang et
548 al., 2017a) and WSOC of LHG glacier from the TP region (~ 700 – 1900) (Feng et al.,
549 2016, 2018), but they are lower than those of WSOC from Antarctica (~ 1400 – 2600)
550 and Greenland ice sheets (~ 1200 – 4400) (Antony et al., 2014; Bhatia et al., 2010).
551

552 **Table 1.** Averages (Arithmetic Mean \pm Standard Deviation) of molecular characteristics in major formula categories detected in ESI+ mode for each group of sites.

553 Numbers and percentages of formulas, intensity weighted MW_w , H/C_w , O/C_w , DBE_w , DBE/C_w , AI_w are given.

	All+	CH+	CHO+	CHON+	CHOS+	CHONS+	CHS+
Number of formulas	1113 \pm 203	48 \pm 6	460 \pm 68	249 \pm 61	121 \pm 33	135 \pm 45	43 \pm 15
Percent of formulas (%)		4 \pm 1	42 \pm 5	22 \pm 1	11 \pm 2	12 \pm 2	4 \pm 1
Molecular weight (Da)	231 \pm 9	146 \pm 5	207 \pm 21	211 \pm 15	329 \pm 18	294 \pm 18	257 \pm 13
U Urban/Industrial (n = 14)							
H/C_w	1.51 \pm 0.05	1.31 \pm 0.04	1.72 \pm 0.10	1.73 \pm 0.14	1.12 \pm 0.09	1.70 \pm 0.08	1.11 \pm 0.02
O/C_w	0.19 \pm 0.04	0	0.28 \pm 0.05	0.23 \pm 0.02	0.07 \pm 0.02	0.29 \pm 0.04	0
DBE_w	5.08 \pm 0.60	4.6 \pm 0.47	3.03 \pm 0.66	3.68 \pm 0.68	10.13 \pm 0.70	4.10 \pm 0.44	8.67 \pm 0.63
DBE/C_w	0.34 \pm 0.03	0.44 \pm 0.02	0.24 \pm 0.04	0.34 \pm 0.07	0.49 \pm 0.05	0.35 \pm 0.04	0.51 \pm 0.01
AI_w	0.25 \pm 0.04	0.44 \pm 0.02	0.13 \pm 0.03	0.17 \pm 0.09	0.42 \pm 0.07	0.15 \pm 0.04	0.48 \pm 0.01
Number of formulas	942 \pm 166	45 \pm 11	533 \pm 81	245 \pm 51	25 \pm 15	53 \pm 13	7 \pm 3
Percent of formulas (%)		5 \pm 1	57 \pm 2	26 \pm 2	3 \pm 2	6 \pm 1	0.7 \pm 0.2
Molecular weight (Da)	229 \pm 10	134 \pm 11	239 \pm 12	214 \pm 17	351 \pm 21	260 \pm 20	237 \pm 30
R Remote/Rural (n = 10)							
H/C_w	1.69 \pm 0.04	1.26 \pm 0.08	1.75 \pm 0.04	1.69 \pm 0.10	1.51 \pm 0.04	1.74 \pm 0.08	1.17 \pm 0.12
O/C_w	0.34 \pm 0.01	0	0.39 \pm 0.01	0.27 \pm 0.02	0.10 \pm 0.05	0.26 \pm 0.02	0
DBE_w	3.16 \pm 0.21	4.53 \pm 0.31	2.80 \pm 0.16	4.11 \pm 0.48	6.25 \pm 0.51	3.92 \pm 0.62	7.49 \pm 1.64
DBE/C_w	0.26 \pm 0.02	0.47 \pm 0.04	0.22 \pm 0.02	0.35 \pm 0.05	0.30 \pm 0.02	0.39 \pm 0.03	0.49 \pm 0.06
AI_w	0.12 \pm 0.03	0.47 \pm 0.04	0.07 \pm 0.03	0.18 \pm 0.06	0.19 \pm 0.03	0.15 \pm 0.04	0.45 \pm 0.07
Number of formulas	727 \pm 146	27 \pm 11	407 \pm 106	186 \pm 39	34 \pm 21	33 \pm 4	7 \pm 6
Percent of formulas (%)		4 \pm 1	56 \pm 4	26 \pm 0.3	5 \pm 3	5 \pm 1	1 \pm 1
Molecular weight (Da)	218 \pm 15	138 \pm 3	215 \pm 30	188 \pm 14	330 \pm 11	290 \pm 20	220 \pm 32
S Soil-influenced (n = 3)							
H/C_w	1.73 \pm 0.05	1.33 \pm 0.02	1.84 \pm 0.08	1.75 \pm 0.06	1.35 \pm 0.17	1.73 \pm 0.06	0.92 \pm 0.13
O/C_w	0.33 \pm 0.04	0	0.40 \pm 0.01	0.23 \pm 0.01	0.07 \pm 0.01	0.29 \pm 0.05	0
DBE_w	3.11 \pm 0.45	4.29 \pm 0.13	2.21 \pm 0.53	3.31 \pm 0.06	7.60 \pm 1.56	4.23 \pm 0.18	8.63 \pm 0.34
DBE/C_w	0.25 \pm 0.03	0.44 \pm 0.01	0.18 \pm 0.03	0.32 \pm 0.03	0.38 \pm 0.09	0.36 \pm 0.02	0.61 \pm 0.07
AI_w	0.14 \pm 0.05	0.44 \pm 0.01	0.07 \pm 0.02	0.15 \pm 0.03	0.29 \pm 0.09	0.13 \pm 0.03	0.58 \pm 0.07
Number of formulas	987	51	578	238	10	65	4
Site 120							

(n = 1)	Percent of formulas (%)	5	59	24	1	7	0.4
	Molecular weight (Da)	234	145	245	212	246	250
	H/C_w	1.69	1.29	1.72	1.80	1.95	1.14
	O/C_w	0.32	0	0.37	0.26	0.29	0
	DBE_w	3.36	4.67	3.14	3.54	2.99	8.05
	DBE/C_w	0.26	0.45	0.23	0.30	0.32	0.50
	AI_w	0.11	0.45	0.07	0.12	0.07	0.46

554

Table 2. Averages (Arithmetic Mean \pm Standard Deviation) of molecular characteristics in major formula categories detected in ESI- mode for each group of sites.

555

556 Numbers and percentages of formulas, intensity weighted MW_w , H/C_w , O/C_w , DBE_w , DBE/C_w , AI_w are given.

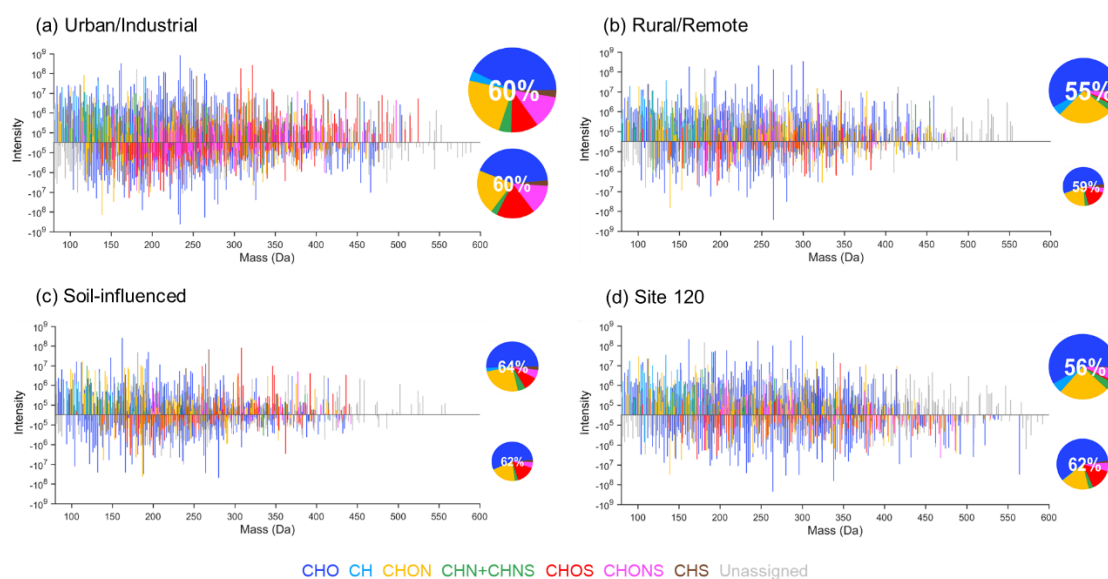
	All-	CHO-	CHON-	CHOS-	CHONS-
Number of formulas	871 \pm 287	404 \pm 112	194 \pm 79	156 \pm 48	82 \pm 49
Percent of formulas (%)	47 \pm 4	22 \pm 2	18 \pm 2	9 \pm 3	252 \pm 24
Molecular weight (Da)	223 \pm 17	229 \pm 19	183 \pm 18	238 \pm 17	1.55 \pm 0.15
H/C_w	1.48 \pm 0.09	1.57 \pm 0.06	1.00 \pm 0.14	1.68 \pm 0.08	0.60 \pm 0.06
O/C_w	0.35 \pm 0.04	0.30 \pm 0.05	0.45 \pm 0.04	0.56 \pm 0.05	4.55 \pm 0.55
DBE_w	4.14 \pm 0.26	3.87 \pm 0.31	5.59 \pm 0.51	3.13 \pm 0.42	0.46 \pm 0.08
DBE/C_w	0.38 \pm 0.06	0.30 \pm 0.04	0.72 \pm 0.08	0.29 \pm 0.04	0.14 \pm 0.06
AI_w	0.19 \pm 0.07	0.12 \pm 0.04	0.54 \pm 0.09	0.05 \pm 0.02	34 \pm 16
Number of formulas	537 \pm 92	266 \pm 35	107 \pm 21	100 \pm 29	6 \pm 2
Percent of formulas (%)	50 \pm 4	20 \pm 2	180 \pm 12	241 \pm 22	241 \pm 27
Molecular weight (Da)	215 \pm 21	216 \pm 28	1.03 \pm 0.16	1.76 \pm 0.10	1.52 \pm 0.13
H/C_w	1.44 \pm 0.07	1.54 \pm 0.10	0.42 \pm 0.04	0.58 \pm 0.08	0.65 \pm 0.07
O/C_w	0.39 \pm 0.06	0.37 \pm 0.07	5.43 \pm 0.69	2.68 \pm 0.86	4.30 \pm 0.79
DBE_w	4.09 \pm 0.31	3.70 \pm 0.65	0.72 \pm 0.10	0.25 \pm 0.06	0.49 \pm 0.07
DBE/C_w	0.42 \pm 0.05	0.33 \pm 0.05	0.60 \pm 0.14	0.04 \pm 0.04	0.16 \pm 0.06
AI_w	0.26 \pm 0.05	0.13 \pm 0.05	85 \pm 18	69 \pm 9	22 \pm 6
Number of formulas	438 \pm 84	245 \pm 53	85 \pm 18	69 \pm 9	5 \pm 1
Percent of formulas (%)	56 \pm 2	19 \pm 1	16 \pm 2	16 \pm 2	5 \pm 1

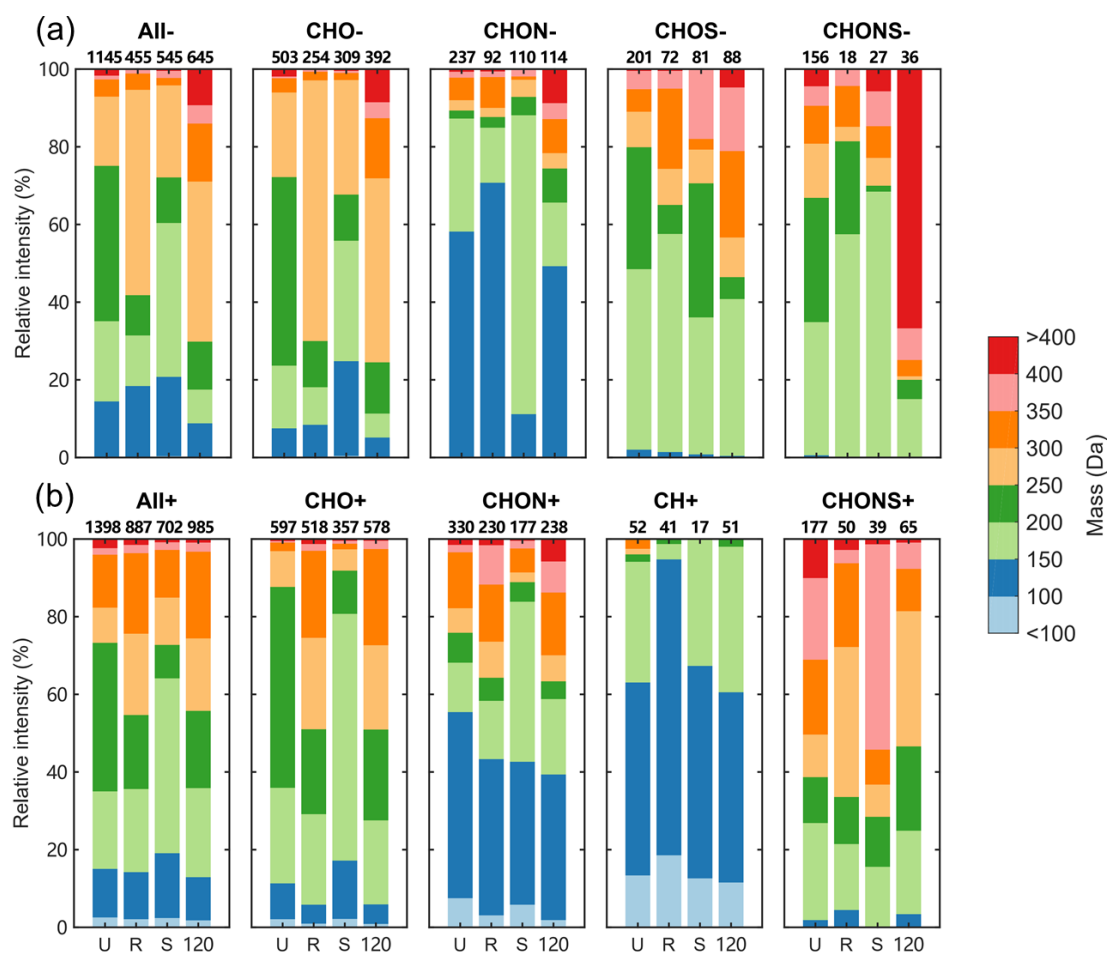
(n = 3)	Molecular weight (Da)	206±3	195±11	212±27	249±15	228±11
	<i>H/C_w</i>	1.53±0.01	1.53±0.01	1.48±0.23	1.47±0.22	1.76±0.2
	<i>O/C_w</i>	0.41±0.02	0.42±0.03	0.36±0.02	0.42±0.04	0.67±0.03
	<i>DBE_w</i>	3.65±0.07	3.40±0.31	4.43±1.51	4.51±1.29	3.51±0.32
	<i>DBE/C_w</i>	0.36±0.01	0.35±0.00	0.43±0.11	0.37±0.12	0.38±0.09
	<i>AI_w</i>	0.13±0.01	0.12±0.00	0.22±0.10	0.09±0.05	0.13±0.05
	Number of formulas	645	392	114	88	36
	Percent of formulas (%)	61	18	14	14	6
	Molecular weight (Da)	280	286	212	271	396
Site 120	<i>H/C_w</i>	1.41	1.46	0.99	1.51	1.15
(n = 1)	<i>O/C_w</i>	0.34	0.32	0.48	0.50	0.44
	<i>DBE_w</i>	5.63	5.44	6.40	5.19	11.97
	<i>DBE/C_w</i>	0.38	0.34	0.71	0.35	0.59
	<i>AI_w</i>	0.14	0.09	0.53	0.13	0.26

557

558

559 The mass spectra plots constructed from individual samples showing integrated
560 composition of U, R, S, and site 120 samples along with the corresponding number
561 contributions from different formula categories are shown in Fig. 4. Overall, the
562 assigned formulas were mainly in the mass range of 100 to 450 Da for both ESI+ and
563 ESI-, while there were more compounds with masses lower than 100 in the ESI+ mode.
564 The relative intensities of MS features contributed by compounds in different mass
565 ranges extract more information from the mass spectra, as shown in Fig. 5. In ESI-
566 mode, the ion intensity was most abundant in the mass range of 200 to 250 Da for U
567 samples, 250 to 300 Da for R and site 120 samples, and 150 to 200 Da for S samples,
568 indicating different chemical constituents for samples from different groups. The
569 variations in terms of relative intensities for CHO- compounds were like those of all
570 species detected in ESI-. For CHON-, formulas with mass of 150 to 200 Da were
571 abundant in S samples, while other groups were dominant by formulas in the range of
572 100 to 150 Da. Sample from site 120 showed higher fractions of formulas with masses
573 larger than 300 Da, especially for CHONS- compounds. The distributions of all
574 detected compounds showed higher contributions from mass range of 300 to 350 Da in
575 ESI+ compared to ESI-. Although detection of CH compounds in ESI is uncommon,
576 some of them appear detectable in the ESI+ mode, most were associated with aromatic
577 species smaller than 150 Da ($DBE \geq 4$). Furthermore, the CHONS+ species showed
578 higher masses than CHONS-, except for the sample from site 120.
579





588

589 **Figure 5.** The distributions for relative intensities of compounds in different mass ranges in (a) ESI-
 590 and (b) ESI+. The numbers on the top of bars indicate the number of assigned peaks in different
 591 formula categories of each sample.

592

593 In ESI+ mode, CHO+ and CHON+ were the main components in all samples,
 594 accounting for 35% to 61% and 20% to 28% of total formulas, respectively (Table 1).
 595 The U samples showed the lowest CHO+ abundance (mean: 42%±5%) while the
 596 sample from site 120 had the highest value (59%). The fractions of CHON+ species in
 597 our samples were significantly lower than those of the aged firn/ice samples from the
 598 TP (~40%) (Feng et al., 2016, 2018, 2020; Spencer et al., 2014) which is mainly
 599 attributed to less microbial activities in our samples; but were comparable with those
 600 of fresh snow (Feng et al., 2018, 2020) in which the major source of WSOC is aerosol

601 wet/dry deposition. These results indicate that WSOC from the snowpack in northern
602 Xinjiang was more likely from atmospheric aerosol depositions rather than from
603 autochthonous sources. There were much higher contributions of S-containing
604 compounds in the U samples, e.g., CHOS⁺ (11%), CHONS⁺ (12%), and CHS⁺ (4%),
605 which were less abundant in other samples. These species showed low oxidation level
606 (mean O/C_w : 0.07 for CHOS⁺), high unsaturation degree and aromaticity (mean DBE_w :
607 10.1 and 8.7; mean AI_w : 0.42 and 0.48 for CHOS⁺ and CHS⁺, respectively), suggesting
608 that they might be reduced S-containing species with aromatic structures from
609 incomplete fossil fuel combustion (Mead et al., 2015; Wang et al., 2017a).

610 The abundance of CHO⁻ was highest in ESI⁻ with a range of 41% to 61%. The U
611 samples and the site 120 sample showed the lowest (mean: 47%±4%) and highest (61%)
612 fractions of CHO⁻, respectively. The CHON⁻ and CHOS⁻ compounds account for
613 roughly equal contributions with ranges of 16% to 27% and 14% to 22%, respectively.
614 The detected CHOS compounds were more abundant in ESI⁻ than those in ESI⁺.
615 Furthermore, CHOS⁻ compounds show much higher oxidation level and lower
616 unsaturation degrees than CHOS⁺ (mean O/C_w : 0.55 and 0.08; mean DBE : 8.3 and 3.2
617 for CHOS⁻ and CHOS⁺, respectively). These results are consistent with previous
618 ambient aerosol characterization studies (Lin et al., 2012; Wang et al., 2017a, 2018), but
619 the S-containing species were not abundantly detected in the glacier samples (Feng et
620 al., 2016; Spencer et al., 2014), indicating stronger influence from anthropogenic
621 aerosols to WSOC in Xinjiang seasonal snow than those from remote areas.

622 The bulk molecular characteristics of compounds detected in ESI⁺ and ESI⁻ are
623 summarized in Tables 1 and 2, respectively. The MW_w of all compounds detected in
624 ESI⁺ mode was 231±9 Da, 229±10 Da, 218±15 Da, and 234 Da for U, R, S, and site
625 120 samples, respectively. These values are comparable with the MW_w of urban aerosols

626 (~225 to 265 Da) (Lin et al., 2012; Wang et al., 2018), but significantly lower than those
627 of glacier samples (~360 Da to 420 Da) (Feng et al., 2018, 2020), suggesting different
628 compositions between WSOC in seasonal snow of our study and from the literature
629 reported glacier samples. *DBE* is used to infer the unsaturation degree of individual
630 species (McLafferty et al., 1993) and *AI* is a more direct metric of their aromaticity
631 (Koch and Dittmar, 2006, 2016). The U samples showed higher *DBE_w* and *AI_w* values
632 than the other groups of samples mainly due to high fractions of S-containing
633 compounds in ESI+ mode (Table 1). As for ESI- mode, the *MW_w* of the site 120 sample
634 was higher than the other samples (280 Da vs. ~200 – 220 Da). Of note, the average
635 *MW_w* of CHO- and CHONS- compounds in the site 120 sample were 286 Da and 396
636 Da, respectively, which were approximately 70 Da and 150 Da higher than those from
637 the other groups of samples. Accordingly, the *DBE_w* of all formulas detected in the site
638 120 sample was the highest (5.8), the values for CHO- and CHONS- were 5.4 and 12.0,
639 respectively, which were approximately 1.5 and 3 times higher than in the other samples.
640 These results indicate very unusual sources of WSOC in the site 120 sample.
641 Additionally, the molecular characteristics of formulas detected in ESI- and ESI+ are
642 different, e.g., higher average *DBE_w* and *AI_w* values of R samples for ESI- data (Tables
643 1 and 2). This results from the differences of ionization mechanisms between positive
644 and negative modes. ESI+ is sensitive to protonatable compounds with basic functional
645 groups, while acidic species are easily deprotonated and detected in ESI- mode (Cech
646 and Enke, 2001). Therefore, using both positive and negative ESI modes provide a more
647 complete molecular characterization of WSOC.

648

649

650

651 3.3.2 Chemical species in snow WSOC

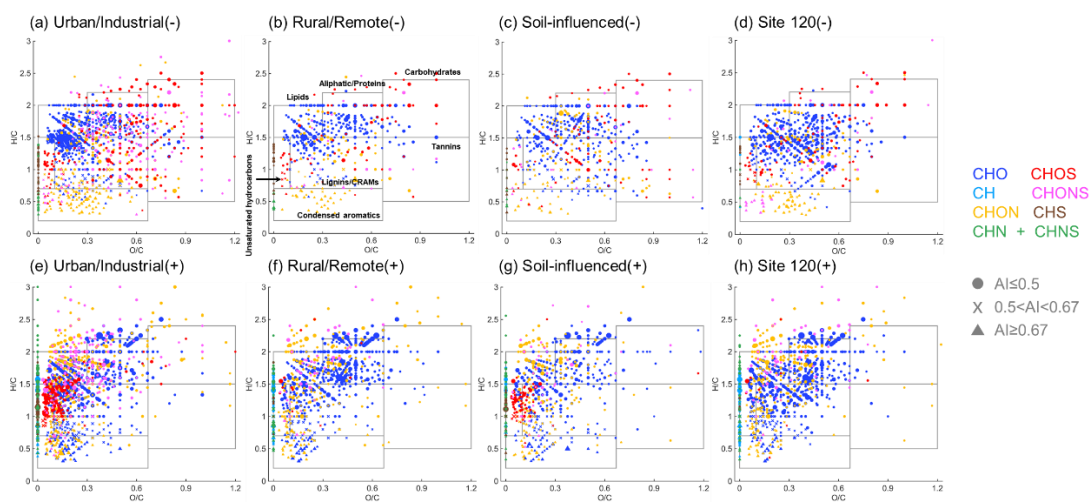
652 The Van Krevelen (VK) diagram is a frequently used graphical method, which plots
653 the H/C ratios against the O/C ratios in molecular formulas, to qualitatively determine
654 the major chemical species in complex organic mixtures and to explore their potential
655 reaction pathways (Kim et al., 2003). The VK diagrams of four representative samples
656 detected in ESI+ and ESI- modes are shown in Fig. 6. The VK space in this study was
657 separated into seven regions according to previous studies (Feng et al., 2016; Ohno et
658 al., 2010): (1) lipids-like ($O/C = 0-0.3$, $H/C = 1.5-2.0$), (2) aliphatic/proteins-like (O/C
659 $= 0.3-0.67$, $H/C = 1.5-2.2$), (3) carbohydrates-like ($O/C=0.67-1.2$; $H/C=1.5-2.4$), (4)
660 unsaturated hydrocarbons ($O/C = 0-0.1$, $H/C = 0.7-1.5$), (5) lignins/carboxylic-rich
661 alicyclic molecules (CRAMs)-like ($O/C = 0.1-0.67$, $H/C = 0.7-1.5$), (6) tannins-like
662 ($O/C = 0.67-1.2$, $H/C = 0.5-1.5$), and (7) condensed aromatics ($O/C = 0-0.67$, $H/C =$
663 $0.2-0.7$). In ESI+, the U samples showed the lowest O/C ratios (mean: 0.19 ± 0.04) and
664 H/C ratios (mean: 1.51 ± 0.05) among four groups (Table 1), which indicate low
665 oxygenation and high unsaturation degree of WSOC from U samples, likely suggesting
666 their primary emission sources (Kroll et al., 2011). Consequently, the unsaturated
667 hydrocarbons were most abundant among seven classes of species (mean: $39\pm 15\%$,
668 Table 3), most of which were CHOS+ compounds (Fig. S7), then followed by
669 lignins/CRAMs-like species (mean: $25\pm 11\%$). These results, again, supports our
670 assumption that anthropogenic pollution is a major source of snow organics in the U
671 region. The R samples exhibited the highest fraction of aliphatic/proteins-like species
672 among four groups (mean: $57\%\pm 4\%$). This type of species is widely distributed in
673 natural dissolved organic matter detected in terrestrial water systems (Lu et al., 2015a),
674 glaciers and polar ice sheets (Antony et al., 2014; Feng et al., 2016), aerosols (Ning et
675 al., 2019; Wu et al., 2019a; Xie et al., 2020), and cloud water (Bianco et al., 2018). The

676 aliphatic/proteins-like species is commonly regarded as a marker of biological-related
677 sources, such as in-situ microbial activities (Antony et al., 2017) and primary
678 bioaerosols (e.g., plant debris, fungal spores, and pollen) (Xie et al., 2020). The high
679 contribution of aliphatic/proteins-like species in R samples is consistent with the results
680 of our EEM-PARAFAC analysis, which showed that PRLIS fluorophore is the most
681 abundant. The U samples and the site 120 sample showed high contributions of
682 lignins/CRAMs-like species, but their sources might be different. The lignins/CRAMs-
683 like species are commonly attributed to terrestrial-sourced, vascular plant-derived
684 material (Antony et al., 2014), biomolecules with similar structures to sterols and
685 hopanoids (Hertkorn et al., 2006), or secondary organic aerosols from biomass burning
686 (Xie et al., 2020). These compounds in U samples were more likely from combustion
687 of biomass materials, but those in the site 120 sample might be from biogenetic sources.
688 In addition, the S samples showed higher contributions of unsaturated hydrocarbons
689 (mean: $19\% \pm 14\%$) than the R samples and the site 120 sample (mean: $11\% \pm 2\%$ and
690 10% , respectively). This result is mainly due to the CHOS⁺ compounds detected in the
691 site 104 sample from R group (Fig. 6g), indicating some influence by anthropogenic
692 pollution at this site.

693

694

695



696

697 **Figure 6.** Van Krevelen diagrams of representative sample for each subgroup in (a-d) ESI- and
 698 h) ESI+. The boxes indicate the different classes of chemical species. Different formula categories
 699 are color coded. Dots, crosses, and triangles represent non-aromatic ($AI \leq 0.5$), aromatic
 700 ($0.5 < AI < 0.67$), and condensed aromatic compounds ($AI \geq 0.67$) (Koch and Dittmar, 2006),
 701 respectively. The sizes of the symbols are proportional to the intensities.

702

Table 3. The relative abundance of different classes of molecular species in each group of sites.

		%Lipids-like	%Aliphatic/ protein-like	%Carbohydrates- like	%Unsaturated hydrocarbons	%Lignins/ CRAMs-like	%Tannins-like	%Condensed aromatics
U Urban/ Industrial (n = 14)	ESI+	18±9	15±12	0.2±0.1	39±15	25±11	0	3±3
	ESI-	11±13	24±7	4±1	1±0.4	56±12	3±1	1±0.4
R Rural/Remote (n = 10)	ESI+	12±4	57±4	0.7±0.2	11±2	14±3	0.1	5±5
	ESI-	10±7	27±8	5±1	2±2	50±16	3±1	3±3
S Soil-influenced (n = 3)	ESI+	15±2	47±22	0.5±0.1	19±14	14±5	0.1	6±1
	ESI-	9±5	41±1	5±1	1±0.1	39±5	3±2	2±0.1
Site 120 (n = 1)	ESI+	14	52	0.4	10	22	0.1	1
	ESI-	6	13	2	2	75	0.8	2

706 The relative abundances of seven chemical species to four major formula categories
707 are shown in Fig. S7. Aliphatic/proteins-like species dominated the CHO⁺ compounds
708 in the R and the site 120 samples, while lignins/CRAMs-like species were most
709 abundant in the U sample. The contribution of condensed aromatics to CHO⁺ in the S
710 sample was high, which might be from soil-derived humic acids (DiDonato et al.,
711 2016;Ikeya et al., 2015). Lipids-like species were highly enriched in CHON⁺, except
712 for the U samples, in which significantly higher contributions from condensed
713 aromatics were observed. The condensed aromatics have typical AI values > 0.67 and
714 low O/C ratios which might be indicative of nitrated polycyclic aromatic hydrocarbons
715 (niro-PAHs) (Bandowe and Meusel, 2017) or N-heterocyclic aromatics (Bandowe et al.,
716 2016) from combustion sources. The CHOS⁺ compounds have mostly unsaturated
717 hydrocarbons characteristics in representative U and S samples as discussed above but
718 were rarely detected in the R and site 120 samples. The CHONS⁺ did not show distinct
719 variations among investigated samples, but higher fraction of aliphatic/proteins-like
720 species in the S sample was observed.

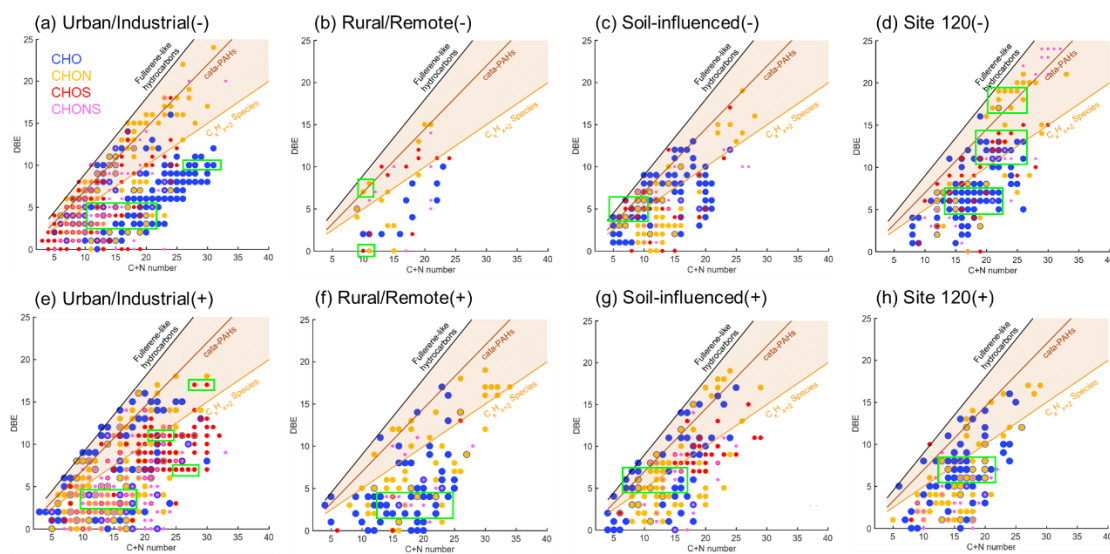
721 As for ESI⁻, the *O/C* (mean: 0.41±0.02) and *H/C* (mean: 1.53±0.01) ratios were
722 highest for species identified in the S samples, reflecting their higher oxygenation and
723 saturation levels. These values are similar to those of soil water extracted organic matter
724 (Ohno et al., 2010). This future is consistent with the results of EEM-PARAFAC, which
725 showed that highly-oxygenated HULIS-1 dominates in S samples. Lignins/CRAMs-
726 like species detected in ESI⁻ dominated the VK space rather than aliphatic/proteins-like
727 compounds detected in ESI⁺. The relative contributions of seven chemical classes did
728 not change much between U and R samples (Table 3). In S samples, lower fraction of
729 lignins/CRAMs-like species was found. Compared to the water extracted organic
730 matter from pure soil sample (Ohno et al., 2010), our S samples showed similar

731 percentage of lignins/CRAMs-like species (39% vs. 44%). An extremely high
732 contribution of lignins/CRAMs-like species (75%) was observed for the site 120 sample,
733 strongly suggesting influence from biogenetic materials. As for the relative abundances
734 in major formula categories, CHO- and CHON- were dominated by lignins/CRAMs-
735 like species, except CHON- of the S sample, which exhibited highest fraction of
736 aliphatic/proteins-like species. This highest CHON- fraction mainly resulted from a
737 single compound with disproportionally high ion abundance, i.e., $C_9H_{17}O_3N$, which
738 might be tentatively assigned as amino acid and led to a high fraction of
739 aliphatic/proteins-like compounds in S samples (mean: $41\% \pm 1\%$). Amino acids are
740 widely distributed in soil and are important organic nitrogen sources of soil
741 microorganisms and plants (Geisseler et al., 2010). Moreover, biomass burning is also
742 a significant source of atmospheric amino acids (Laskin et al., 2009; Lin et al., 2012).
743 Therefore, either deposition of blowing soil or biomass burning aerosols may be
744 responsible for the appearance of this high-abundance amino acid species in the S
745 sample. As for CHOS- and CHONS-, lignins/CRAMs-like and carbohydrates-like
746 species accounted for large portions of their total intensity. Only a few CHONS-
747 compounds are apportioned as lignins/CRAMs-like species for the S sample, they are
748 attributed mostly to carbohydrates-like species than anything else. One interesting note
749 is that the contribution of condensed aromatics in the site 120 sample is highest among
750 all samples. Specifically, there are some unique CHONS- compounds within the region
751 of condensed aromatics, e.g., $C_{29}H_{14}O_4N_2S$ (DBE=24, AI=0.77) and $C_{26}H_{14}O_5N_2S$
752 (DBE=21, AI=0.72), which have high MW>400 Da. They may contain structure of
753 anthraquinones, which are widely distributed in nature plants (Duval et al., 2016).

754 To further illustrate the differences of chemical compositions and structures among
755 four groups of the investigated samples, plots of DBE versus C+N atomic number are

756 shown in Fig. 7. The numbers of unique formulas in the U sample were highest both in
757 ESI+ and ESI- with values of 578 and 618 (Fig. S8), respectively, which accounted for
758 44% and 54% of total assigned species in each of the modes. These values were lowest
759 for the R sample, with only 17% (145) and 11% (51) in ESI+ and ESI-, respectively.
760 These results reflect very high chemical complexity of WSOC from U samples. The
761 DBE plots of Fig. 7 are shown along with the reference lines depicting DBE values
762 characteristic of (a) linear polyenes (C_xH_{x+2} , $DBE = 0.5 \times C$) (Cain et al., 2014); (b)
763 cata-condensed PAHs ($DBE = 0.75 \times C - 0.5$) (Siegmann and Sattler, 2000); (c)
764 fullerene-like hydrocarbons ($DBE = 0.9 \times C$) (Lobodin et al., 2012). Because efficient
765 absorption of visible light by organic molecules requires conjugated group of bonds
766 extended across a significant part of the molecule, the compounds with the DBE/C
767 greater than that of linear polyenes might be potential chromophores (Lin et al., 2018).
768 The DBE values of CHON and CHONS compounds shift 1–5 units to the right as the
769 sum-total number of carbon and nitrogen atoms are accounted for. In ESI-, 266
770 formulas of the U sample were in the “BrC domain” region, which was much higher
771 than the other samples (26, 106, and 115 for the R, S, and site 120 sample, respectively).
772 Most of them are CHON-, CHOS- and CHONS- compounds, accounting for 74% of
773 the total formulas assigned in the U sample. Their C numbers and DBE values were
774 mainly in the ranges of 4-16 and 4-10, respectively. For the S and site 120 samples,
775 CHO- and CHON- were abundant in the “BrC domain” region (70% and 62% for the
776 S and site 120 samples, respectively). The frequency distributions of C numbers and
777 DBE were similar between the U and S samples, but WSOC components in the S
778 samples showed higher O/C ratios for CHO- compounds (Fig. S9), again consistent
779 with the soil organic matter (Ohno et al., 2010). However, the observations are quite
780 different for the site 120 sample, where C numbers and DBE values gathered in broader

781 ranges of 11-26 and 10-20, respectively, with higher medians. In addition, a few of the
 782 CHON- and CHONS- compounds with DBE higher than 17 were detected. These
 783 CHONS- formulas have been identified as plant-related organics as discussed above.
 784 Similarly, the highly unsaturated CHON- compounds, e.g., $C_{25}H_{13}O_8N$ (DBE=20,
 785 AI=0.69), $C_{26}H_{15}O_8N$ (DBE=20, AI=0.65), and $C_{26}H_{15}O_9N$ (DBE=20, AI=0.63),
 786 showed high MW>400 Da, and they may also be tentatively assigned as anthraquinone
 787 derivatives. All these unique compounds suggested that the biogenic organics from
 788 plants are major sources of WSOC from the site 120 sample. In ESI+, the numbers of
 789 formulas within “BrC domain” were 216, 43, 103, and 64 for the U, R, S, and site 120
 790 samples, respectively. These potential BrC species were largely attributed to CHO+ and
 791 CHON+ compounds (54%-75%), whereas the S-containing compounds (34%) were
 792 substantial in the U sample.



793
 794 **Figure 7.** DBE vs. C+N number for unique molecules in representative samples from different
 795 groups. (a-d) ESI- and (e-h) ESI+. The reference lines indicate linear polyenes (C_xH_{x+2} , $DBE = 0.5$
 796 $\times C$), cata-condensed PAHs ($DBE = 0.75 \times C - 0.5$), and fullerene-like hydrocarbons ($DBE = 0.9 \times$
 797 C). Markers in the shaded area are potential BrC chromophores. The green boxes denote the high-
 798 intensity compounds. Four major formula categories are shown in different colors and sizes to avoid
 799 overlapping.

800 **3.4 The radiative forcing by BrC attributed to WSOC in the snowpack**

801 Inherent to the complexity of WSOC material and variability of its BrC optical
802 properties, quantitative estimates of its RF in snowpack remain insufficiently studied.
803 Yan et al. (2016) calculated the BrC-induced RF at LHG glacier from the TP region,
804 which was 0.43 W m^{-2} and accounted for 10% of RF due to BC. Most recently, Beres
805 et al. (2020) described the spectral albedo and RF after artificial deposition of BrC
806 aerosol proxies from peat burning onto ambient snow surface. They showed that the
807 instantaneous RF efficiency due to total deposited aerosol was 1.23 W m^{-2} per ppm of
808 the deposited mass. However, in the real world, BrC concentrations may not be that
809 high as in the proxy experiments. Also, daily averaged values of RF are more important
810 for the climate research. Here we contribute to this line of work by calculating the
811 averaged-daily RF due to BC and BrC ($RF_{BC, BrC}$) deposits in snow based on the bulk
812 characterization measurements over the samples of our study.

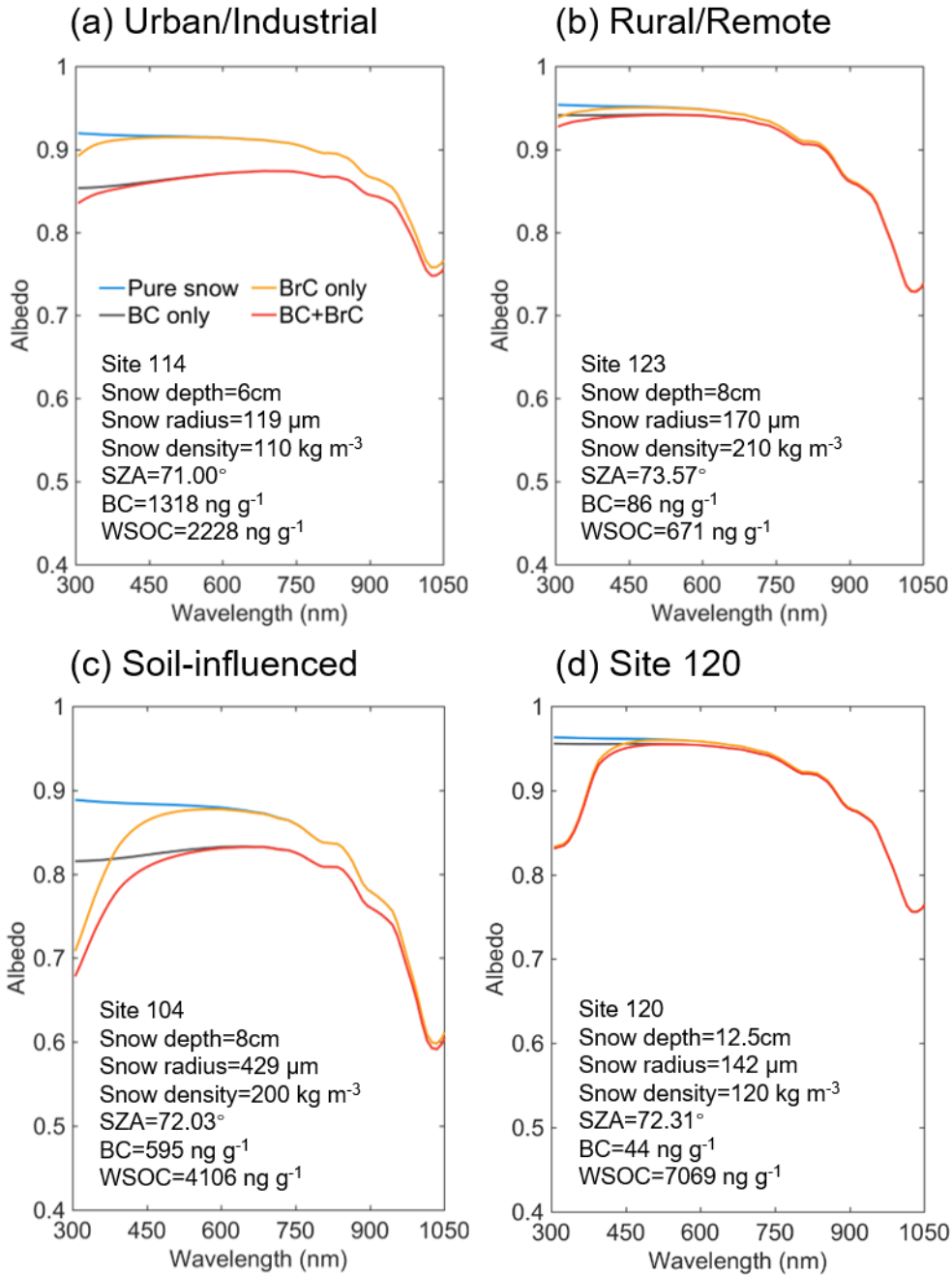
813 Figure 8 shows the snow spectral albedo (α_λ) simulated for four different scenarios,
814 comparing albedo changes of the snowpack containing levels of BC and WSOC
815 measured in the samples. Because most of the snowpack was shallow during the
816 campaign, the albedo of pure snow was influenced by the effects of dark ground surface
817 (albedo assumed to be 0.2) underlying at the snow depth specific to each of the sites,
818 as shown in Fig. 8. The average values of $\Delta\alpha$ and RF due to BC and BrC at different
819 spectral ranges are summarized in Table 4. As expected, BC have strong broadband
820 impact on the snow albedo and corresponding RF effects. Specifically, U and S samples
821 with high BC mass loadings (mean: 707 and 440 ng g^{-1} , respectively) show albedo
822 reduction ($\Delta\alpha_{BC}$) by 0.034 and 0.037 over broad $300\text{-}1500 \text{ nm}$ wavelength range,
823 respectively, and the corresponding RF_{BC} estimates are as high as 3.5 W m^{-2} . In addition,
824 S and site 120 samples with higher WSOC concentrations (mean: 2082 and 7069 ng g^{-1}

825 ¹, respectively) show lower broadband albedo reduction ($\Delta\alpha_{BrC}$) of ~ 0.006 and the
826 corresponding RF_{BrC} of $\sim 0.6 \text{ W m}^{-2}$. Notably, because of the low BC and high WSOC
827 mass loadings in the site 120 sample, its RF_{BrC} estimate is approximately 2 times higher
828 than RF_{BC} . For the other samples (U, R, and S), the RF_{BrC} is still significant with the
829 average ratios of RF_{BrC}/RF_{BC} being at the level of 0.07-0.16. These results indicated that
830 BrC have profound impact on the reduction of the snow albedo in Northern Xinjiang.
831 As shown in Fig. 9, due to the stronger wavelength dependence of BrC absorption, the
832 spectral albedo reduction by BrC increased sharply at shorter wavelengths (300-400
833 nm), where $\Delta\alpha_{BrC}$ can be as large as 29-65% of the $\Delta\alpha_{BC}$ (Table 4). Unlike graphitic-like
834 components of BC, water-soluble part of BrC can trigger photochemical reactions in
835 snow forming reactive oxygen species (Fede and Grannas, 2015; Grannas et al., 2014),
836 catalyzing reaction chemistry and accelerating its kinetics at snow/ice-air interface
837 (Grannas et al., 2014; Hullar et al., 2020). Overall, these results emphasize important
838 role of WSOC and its BrC components on tempering solar radiation balance and
839 modulating environmental chemistry of organics and their air-snow partitioning
840 pertinent to mid-latitude seasonal snowpack.

841

842 **Table 4.** Simulated broadband albedo reduction due to BC and BrC within different wavelength ranges and the ratios between those of BrC and BC. The BC- and BrC-
 843 induced average-daily radiative forcing is also shown.

	Broadband albedo reduction				Radiative forcing			
	300-400 nm		300-1500 nm		BC	BrC		
	BC	BrC	BrC/BC	BC	BrC/BC	(W m ⁻²)		
U								
Industrial/Urban (n = 14)	0.059±0.056	0.015±0.013	0.29±0.19	0.034±0.034	0.002±0.002	0.07±0.06	3.38±3.54	0.21±0.21
R								
Remote/Rural (n = 10)	0.010±0.006	0.003±0.001	0.39±0.16	0.005±0.003	0.0004±0.0002	0.09±0.05	0.53±0.34	0.04±0.03
S								
Soil-influenced (n = 3)	0.069±0.001	0.044±0.025	0.65±0.37	0.037±0.002	0.006±0.003	0.16±0.08	3.49±0.26	0.55±0.28
Site I20 (n = 1)	0.005	0.066	12.02	0.003	0.006	2.16	0.27	0.59



845

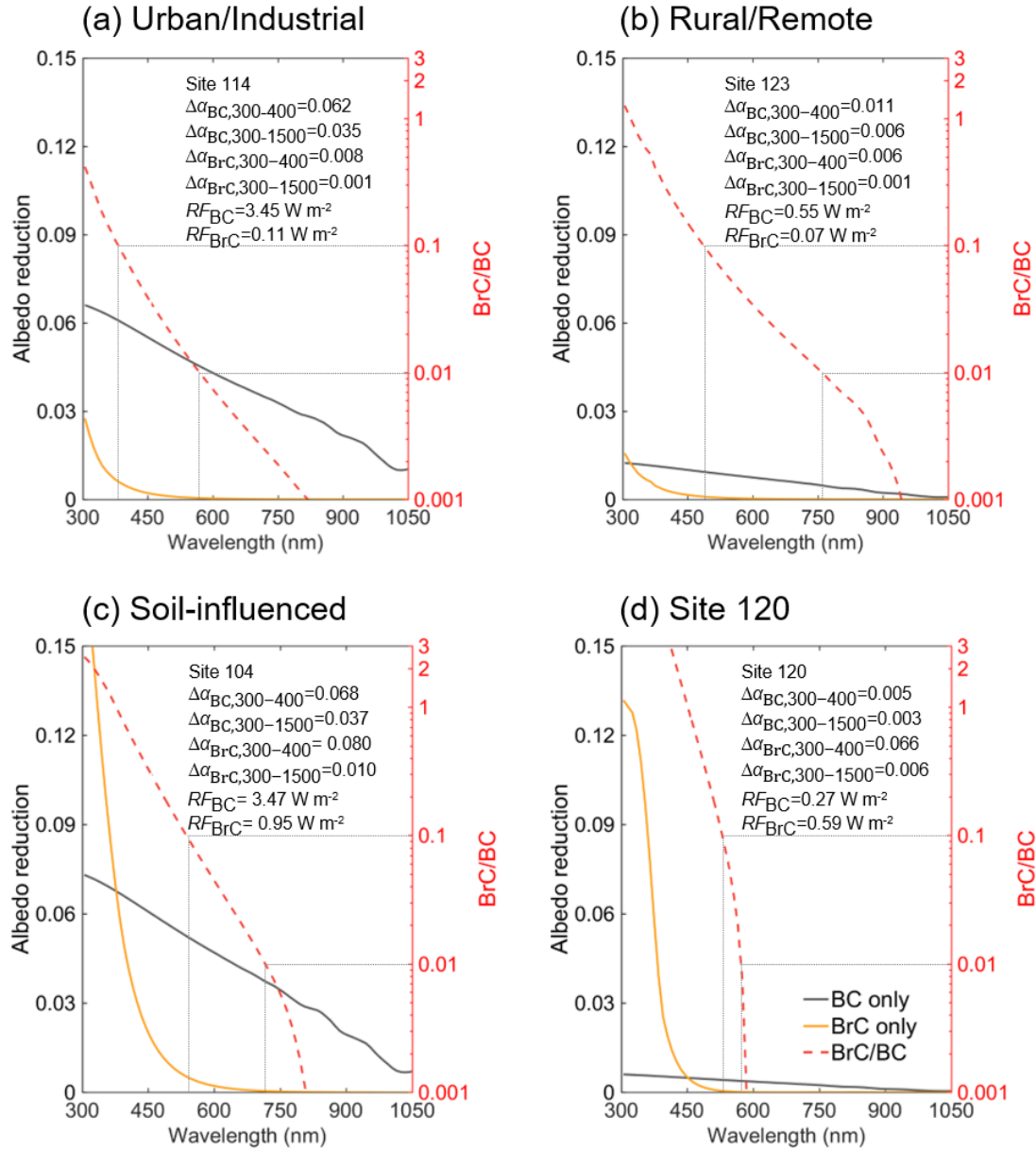
846 **Figure 8.** Simulated snow spectral albedo under different contamination scenarios for representative

847 samples from different groups. The blue, grey, yellow, and red lines exhibit the spectral albedos of

848 pure snow, BC- or BrC-contaminated snow, and snow polluted by both BC and BrC, respectively.

849 The input parameters of each site for SNICAR model are also shown.

850



851

852 **Figure 9.** The albedo reduction spectra for representative samples from different groups. The grey
 853 and yellow lines show the albedo reductions due to BC or BrC, respectively. The red lines show the
 854 ratios of albedo reductions by BrC to those by BC. The $\Delta\alpha_{BC,BrC}$ and $RF_{BC,BrC}$ of each site are also
 855 shown.

856

857 4 Conclusions

858 The concentrations, optical properties, and molecular compositions of WSOC in
 859 seasonal snow collected from 28 sampling sites in Northern Xinjiang, northwestern
 860 China, were measured by multiple analytical techniques. The average concentrations of

861 WSOC were 1968 ± 953 ng g⁻¹, 885 ± 328 ng g⁻¹, 2082 ± 1438 ng g⁻¹, and 7069 ng g⁻¹ for
862 U, R, S, and site 120 samples, respectively, reflecting large variability of WSOC mass
863 loadings among different groups of sites. These values were generally higher than those
864 reported previously for samples from high-altitude or high-latitude regions. Site 120
865 sample showed the highest MAC_{365} (0.95 m² g⁻¹) along with an unusual shape of
866 absorption spectrum, followed by samples from S (0.94 ± 0.31 m² g⁻¹), U (0.39 ± 0.11 m²
867 g⁻¹), and R (0.38 ± 0.12 m² g⁻¹) sites. BrC components of our samples showed either
868 comparable or somewhat lower light-absorbing properties compared to previous reports
869 of polar or glacier snow, and were identified as W-BrC according to the optical-based
870 classification (Saleh, 2020).

871 The differences in bulk chemical composition among four groups of samples were
872 elucidated by EEM spectroscopy assisted with PARAFAC analysis. Terrestrial-sourced
873 HULIS-1 factor accounted for 49% of the total fluorescence in S samples, indicating
874 the significant contributions from soil organic material. HULIS-2 factor dominated the
875 fluorescence intensity of U samples (46%). The anthropogenic sources of HULIS-2
876 were inferred from significantly positive correlation with sulfate ions indicative
877 combustion related sources. PRLIS factor was abundant in R samples (48%), reflecting
878 a potential source of labile WSOC from microbial activities. The EEM map of site 120
879 showed a unique peak never found in any other samples, which might be from plant
880 organics.

881 HPLC-ESI-HRMS provided further information of molecular composition and
882 sources of WSOC. Total, 561 to 1487 and 339 to 1568 formulas were assigned in ESI+
883 and ESI- mass spectra, respectively. The mass distributions with respect to relative
884 intensity were highly variable among representative samples of different groups in both
885 ESI+ and ESI- modes, indicating different composition for each of the samples. CHO+

886 and CHON⁺ were the major components detected in ESI⁺ mode for all samples.
887 CHOS⁺ compounds were highly enriched in U samples. These species had low
888 oxidation degree, high unsaturation level and aromaticity, suggesting S-containing
889 aromatic organics presumably related to heavy fossil fuels. In the ESI⁻ detection mode,
890 CHO⁻ compounds were still dominated, but contribution from CHOS⁻ was much
891 higher, showing roughly equal abundance with CHON⁻. Through analysis of the VK
892 diagrams, the major chemical species in snow WSOC were determined qualitatively.
893 The unsaturated hydrocarbons were the most abundant species in U samples, most of
894 them were CHOS⁺ from anthropogenic emissions. The R samples showed the highest
895 contribution from aliphatic/proteins-like species, which is consistent with the results
896 from EEM-PARAFAC analysis. The S samples showed high oxygenation and
897 saturation degrees, and indicated the similar values of *O/C* and *H/C* ratios and
898 percentage of lignins/CRAMs-like species compared to the soil organic matter (Ohno
899 et al., 2010). An extremely high contribution of lignins/CRAMs-like species were found
900 at the site 120 sample, suggesting the biogenetic sources of WSOC. Furthermore, a few
901 unique CHON⁻ and CHONS⁻ compounds with DBE higher than 17 and MW larger
902 than 400 Da were found at site 120. The most possible candidates for them were species
903 with anthraquinone structures. Therefore, the special spectroscopic features of BrC
904 from the site 120 sample was attributed to biogenic organics from plants.

905 The *RF* due to BrC in snow was reported, for the first time, based on the field data
906 and model simulations. In general, the *RF*_{BrC} were at the levels of 0.04 to 0.59 W m⁻²
907 among different groups of sites and contributed to 7% to 16% of *RF*_{BC}. Therefore, we
908 demonstrated the important influences of WSOC on the snow energy budget and
909 potentially on triggering snow photochemistry. This study presents a comprehensively
910 chemical characterization of WSOC and its BrC properties in collected seasonal snow

911 samples from Northern Xinjiang, northwestern China, which helps to better understand

912 their characteristics, sources, and climate effects.

913

914 *Data availability.* Requests for all data in this study and any questions regarding the
915 data can be directed to Alexander Laskin (alaskin@purdue.edu) or Xin Wang
916 (wxin@lzu.edu.cn).

917

918 *Author contributions.* YZ, CW, AH, XN, and HW designed and conducted the lab
919 experiments. YZ processed the data with assist of CW and AH and wrote the paper. XW,
920 YZ, XN, JC, TS, WP, and HW designed and conducted the field campaign, collected
921 the snow samples, and discussed the results. AL and XW supervised this study. All co-
922 authors commented on the paper and improved it.

923

924 *Competing interests.* The authors declare that they have no conflict of interest.
925

926 *Acknowledgments.* Lanzhou University group acknowledges support from the National
927 Science Fund for Distinguished Young Scholars (42025102) and the National Natural
928 Science Foundation of China (41975157). Purdue group acknowledges support from
929 the Purdue Climate Change Research Center and the US Department of Energy's (DOE)
930 Atmospheric System Research program, Office of Biological and Environmental
931 Research (OBER), award DE-SC0018948. YZ acknowledges support from China
932 Scholarship Council.

933

934 **References**

935

- 936 Amoroso, A., Domine, F., Esposito, G., Morin, S., Savarino, J., Nardino, M.,
 937 Montagnoli, M., Bonneville, J. M., Clement, J. C., Ianniello, A., and Beine, H. J.:
 938 Microorganisms in Dry Polar Snow Are Involved in the Exchanges of Reactive
 939 Nitrogen Species with the Atmosphere, *Environ. Sci. Technol.*, 44, 714-719,
 940 10.1021/es9027309, 2010.
- 941 Anastasio, C., and Robles, T.: Light absorption by soluble chemical species in Arctic
 942 and Antarctic snow, *J. Geophys. Res. Atmos.*, 112, D24304,
 943 10.1029/2007JD008695, 2007.
- 944 Andreae, M. O., and Gelencser, A.: Black carbon or brown carbon? The nature of light-
 945 absorbing carbonaceous aerosols, *Atmos. Chem. Phys.*, 6, 3131-3148,
 946 10.5194/acp-6-3131-2006, 2006.
- 947 Antony, R., Grannas, A. M., Willoughby, A. S., Sleighter, R. L., Thamban, M., and
 948 Hatcher, P. G.: Origin and Sources of Dissolved Organic Matter in Snow on the
 949 East Antarctic Ice Sheet, *Environ. Sci. Technol.*, 48, 6151-6159,
 950 10.1021/es405246a 2014.
- 951 Antony, R., Willoughby, A. S., Grannas, A. M., Catanzano, V., Sleighter, R. L.,
 952 Thamban, M., Hatcher, P. G., and Nair, S.: Molecular Insights on Dissolved
 953 Organic Matter Transformation by Supraglacial Microbial Communities, *Environ.*
 954 *Sci. Technol.*, 51, 4328-4337, 10.1021/acs.est.6b05780, 2017.
- 955 Bandowe, B. A., Meusel, H., Huang, R., Hoffmann, T., Cao, J., and Ho, K.: Azaarenes
 956 in fine particulate matter from the atmosphere of a Chinese megacity, *Environ. Sci.*
 957 *Pollut. Res. Int.*, 23, 16025-16036, 10.1007/s11356-016-6740-z, 2016.
- 958 Bandowe, B. A. M., and Meusel, H.: Nitrated polycyclic aromatic hydrocarbons (nitro-
 959 PAHs) in the environment - A review, *Sci. Total Environ.*, 581-582, 237-257,
 960 10.1016/j.scitotenv.2016.12.115, 2017.
- 961 Bartels-Rausch, T., Brigante, M., Elshorbany, Y. F., Ammann, M., D'Anna, B., George,
 962 C., Stemmler, K., Ndour, M., and Kleffmann, J.: Humic acid in ice: Photo-
 963 enhanced conversion of nitrogen dioxide into nitrous acid, *Atmos. Environ.*, 44,
 964 5443-5450, 10.1016/j.atmosenv.2009.12.025, 2010.
- 965 Beine, H., Anastasio, C., Esposito, G., Patten, K., Wilkening, E., Domine, F., Voisin, D.,
 966 Barret, M., Houdier, S., and Hall, S.: Soluble, light-absorbing species in snow at
 967 Barrow, Alaska, *J. Geophys. Res. Atmos.*, 116, D00R05, 10.1029/2011jd016181,
 968 2011.
- 969 Beres, N. D., Sengupta, D., Samburova, V., Khlystov, A. Y., and Moosmüller, H.:
 970 Deposition of brown carbon onto snow: changes in snow optical and radiative
 971 properties, *Atmos. Chem. Phys.*, 20, 6095-6114, 10.5194/acp-20-6095-2020, 2020.
- 972 Bhatia, M. P., Das, S. B., Longnecker, K., Charette, M. A., and Kujawinski, E. B.:
 973 Molecular characterization of dissolved organic matter associated with the
 974 Greenland ice sheet, *Geochim. Cosmochim. Acta*, 74, 3768-3784,
 975 10.1016/j.gca.2010.03.035, 2010.
- 976 Bianco, A., Deguillaume, L., Vaitilingom, M., Nicol, E., Baray, J. L., Chaumerliac, N.,
 977 and Bridoux, M.: Molecular Characterization of Cloud Water Samples Collected
 978 at the Puy de Dome (France) by Fourier Transform Ion Cyclotron Resonance Mass
 979 Spectrometry, *Environ. Sci. Technol.*, 52, 10275-10285, 10.1021/acs.est.8b01964,
 980 2018.
- 981 Birdwell, J. E., and Valsaraj, K. T.: Characterization of dissolved organic matter in
 982 fogwater by excitation-emission matrix fluorescence spectroscopy, *Atmos.*
 983 *Environ.*, 44, 3246-3253, 10.1016/j.atmosenv.2010.05.055, 2010.

984 Bond, T. C., and Bergstrom, R. W.: Light absorption by carbonaceous particles: An
985 investigative review, *Aerosol Sci. Technol.*, 40, 27-67,
986 10.1080/02786820500421521, 2006.

987 Bond, T. C., Doherty, S. J., Fahey, D. W., Forster, P. M., Berntsen, T., DeAngelo, B. J.,
988 Flanner, M. G., Ghan, S., Karcher, B., Koch, D., Kinne, S., Kondo, Y., Quinn, P.
989 K., Sarofim, M. C., Schultz, M. G., Schulz, M., Venkataraman, C., Zhang, H.,
990 Zhang, S., Bellouin, N., Guttikunda, S. K., Hopke, P. K., Jacobson, M. Z., Kaiser,
991 J. W., Klimont, Z., Lohmann, U., Schwarz, J. P., Shindell, D., Storelvmo, T.,
992 Warren, S. G., and Zender, C. S.: Bounding the role of black carbon in the climate
993 system: A scientific assessment, *J. Geophys. Res. Atmos.*, 118, 5380-5552,
994 10.1002/jgrd.50171, 2013.

995 Brutel-Vuilmet, C., Menegoz, M., and Krinner, G.: An analysis of present and future
996 seasonal Northern Hemisphere land snow cover simulated by CMIP5 coupled
997 climate models, *The Cryosphere*, 7, 67-80, 10.5194/tc-7-67-2013, 2013.

998 Cain, J., Laskin, A., Kholghy, M. R., Thomson, M. J., and Wang, H.: Molecular
999 characterization of organic content of soot along the centerline of a coflow
1000 diffusion flame, *Phys. Chem. Chem. Phys.*, 16, 25862-25875,
1001 10.1039/c4cp03330b, 2014.

1002 Cech, N. B., and Enke, C. G.: Practical implications of some recent studies in
1003 electrospray ionization fundamentals, *Mass Spectrom. Rev.*, 20, 362-387,
1004 10.1002/mas.10008, 2001.

1005 Chen, Q., Mu, Z., Song, W., Wang, Y., Yang, Z., Zhang, L., and Zhang, Y. L.: Size-
1006 Resolved Characterization of the Chromophores in Atmospheric Particulate
1007 Matter From a Typical Coal-Burning City in China, *J. Geophys. Res. Atmos.*, 124,
1008 10546-10563, 10.1029/2019jd031149, 2019.

1009 Chen, Q., Li, J., Hua, X., Jiang, X., Mu, Z., Wang, M., Wang, J., Shan, M., Yang, X.,
1010 Fan, X., Song, J., Wang, Y., Guan, D., and Du, L.: Identification of species and
1011 sources of atmospheric chromophores by fluorescence excitation-emission matrix
1012 with parallel factor analysis, *Sci. Total Environ.*, 718, 137322,
1013 10.1016/j.scitotenv.2020.137322, 2020.

1014 Chen, Q. C., Ikemori, F., and Mochida, M.: Light Absorption and Excitation-Emission
1015 Fluorescence of Urban Organic Aerosol Components and Their Relationship to
1016 Chemical Structure, *Environ. Sci. Technol.*, 50, 10859-10868,
1017 10.1021/acs.est.6b02541, 2016a.

1018 Chen, Q. C., Miyazaki, Y., Kawamura, K., Matsumoto, K., Coburn, S., Volkamer, R.,
1019 Iwamoto, Y., Kagami, S., Deng, Y. G., Ogawa, S., Ramasamy, S., Kato, S., Ida, A.,
1020 Kajii, Y., and Mochida, M.: Characterization of Chromophoric Water-Soluble
1021 Organic Matter in Urban, Forest, and Marine Aerosols by HR-ToF-AMS Analysis
1022 and Excitation Emission Matrix Spectroscopy, *Environ. Sci. Technol.*, 50, 10351-
1023 10360, 10.1021/acs.est.6b01643, 2016b.

1024 Chen, Y., and Bond, T. C.: Light absorption by organic carbon from wood combustion,
1025 *Atmos. Chem. Phys.*, 10, 1773-1787, 10.5194/acp-10-1773-2010, 2010.

1026 Coble, P. G.: Characterization of marine and terrestrial DOM in seawater using
1027 excitation emission matrix spectroscopy, *Mar. Chem.*, 51, 325-346, 10.1016/0304-
1028 4203(95)00062-3, 1996.

1029 Coble, P. G., Del Castillo, C. E., and Avril, B.: Distribution and optical properties of
1030 CDOM in the Arabian Sea during the 1995 Southwest Monsoon, *Deep-Sea Res.*
1031 Pt. II, 45, 2195-2223, 10.1016/S0967-0645(98)00068-X, 1998.

1032 Cook, J. M., Hodson, A. J., Gardner, A. S., Flanner, M., Tedstone, A. J., Williamson, C.,
1033 Irvine-Fynn, T. D. L., Nilsson, J., Bryant, R., and Tranter, M.: Quantifying

1034 bioalbedo: a new physically based model and discussion of empirical methods for
1035 characterising biological influence on ice and snow albedo, *Cryosphere*, 11, 2611-
1036 2632, 10.5194/tc-11-2611-2017, 2017a.

1037 Cook, J. M., Hodson, A. J., Taggart, A. J., Mernild, S. H., and Tranter, M.: A predictive
1038 model for the spectral "bioalbedo" of snow, *J. Geophys. Res. Earth*, 122, 434-454,
1039 10.1002/2016JF003932, 2017b.

1040 DiDonato, N., Chen, H., Waggoner, D., and Hatcher, P. G.: Potential origin and
1041 formation for molecular components of humic acids in soils, *Geochim.*
1042 *Cosmochim. Acta* 178, 210-222, 10.1016/j.gca.2016.01.013, 2016.

1043 Doherty, S. J., Warren, S. G., Grenfell, T. C., Clarke, A. D., and Brandt, R. E.: Light-
1044 absorbing impurities in Arctic snow, *Atmos. Chem. Phys.*, 10, 11647-11680,
1045 10.5194/acp-10-11647-2010, 2010.

1046 Duarte, R. M. B. O., Santos, E. B. H., Pio, C. A., and Duarte, A. C.: Comparison of
1047 structural features of water-soluble organic matter from atmospheric aerosols with
1048 those of aquatic humic substances, *Atmos. Environ.* , 41, 8100-8113,
1049 10.1016/j.atmosenv.2007.06.034, 2007.

1050 Duval, J., Pecher, V., Pujol, M., and Lesellier, E.: Research advances for the extraction,
1051 analysis and uses of anthraquinones: A review, *Ind. Crops Prod.*, 94, 812-833,
1052 10.1016/j.indcrop.2016.09.056, 2016.

1053 Elliott, A., Mundy, C. J., Gosselin, M., Poulin, M., Campbell, K., and Wang, F.: Spring
1054 production of mycosporine-like amino acids and other UV-absorbing compounds
1055 in sea ice-associated algae communities in the Canadian Arctic, *Mar. Ecol. Prog.*
1056 *Ser.*, 541, 91-104, 10.3354/meps11540, 2015.

1057 Fede, A., and Grannas, A. M.: Photochemical Production of Singlet Oxygen from
1058 Dissolved Organic Matter in Ice, *Environ. Sci. Technol.*, 49, 12808-12815,
1059 10.1021/acs.est.5b03600, 2015.

1060 Fellman, J. B., Hood, E., Raymond, P. A., Stubbins, A., and Spencer, R. G. M.: Spatial
1061 Variation in the Origin of Dissolved Organic Carbon in Snow on the Juneau
1062 Icefield, Southeast Alaska, *Environ. Sci. Technol.*, 49, 11492-11499,
1063 10.1021/acs.est.5b02685, 2015.

1064 Feng, L., Xu, J. Z., Kang, S. C., Li, X. F., Li, Y., Jiang, B., and Shi, Q.: Chemical
1065 Composition of Microbe-Derived Dissolved Organic Matter in Cryoconite in
1066 Tibetan Plateau Glaciers: Insights from Fourier Transform Ion Cyclotron
1067 Resonance Mass Spectrometry Analysis, *Environ. Sci. Technol.*, 50, 13215-13223,
1068 10.1021/acs.est.6b03971, 2016.

1069 Feng, L., An, Y., Xu, J., and Kang, S.: Characteristics and sources of dissolved organic
1070 matter in a glacier in the northern Tibetan Plateau: differences between different
1071 snow categories, *Ann. Glaciol.*, 59, 31-40, 10.1017/aog.2018.20, 2018.

1072 Feng, L., An, Y., Xu, J., Li, X., Jiang, B., and Liao, Y.: Biochemical evolution of
1073 dissolved organic matter during snow metamorphism across the ablation season
1074 for a glacier on the central Tibetan Plateau, *Sci. Rep.*, 10, 6123, 10.1038/s41598-
1075 020-62851-w, 2020.

1076 Flanner, M. G., Zender, C. S., Randerson, J. T., and Rasch, P. J.: Present-day climate
1077 forcing and response from black carbon in snow, *J. Geophys. Res. Atmos.*, 112,
1078 D11202, 10.1029/2006jd008003, 2007.

1079 Fu, P. Q., Kawamura, K., Chen, J., Qin, M. Y., Ren, L. J., Sun, Y. L., Wang, Z. F., Barrie,
1080 L. A., Tachibana, E., Ding, A. J., and Yamashita, Y.: Fluorescent water-soluble
1081 organic aerosols in the High Arctic atmosphere, *Sci. Rep.*, 5, 9845,
1082 10.1038/Srep09845, 2015.

1083 Ganey, G. Q., Loso, M. G., Burgess, A. B., and Dial, R. J.: The role of microbes in

1084 snowmelt and radiative forcing on an Alaskan icefield, *Nat. Geosci.*, 10, 754-759,
1085 10.1038/ngeo3027, 2017.

1086 Geisseler, D., Horwath, W. R., Joergensen, R. G., and Ludwig, B.: Pathways of nitrogen
1087 utilization by soil microorganisms – A review, *Soil Biol. Biochem.*, 42, 2058-2067,
1088 10.1016/j.soilbio.2010.08.021, 2010.

1089 Grannas, A. M., Jones, A. E., Dibb, J., Ammann, M., Anastasio, C., Beine, H. J., Bergin,
1090 M., Bottenheim, J., Boxe, C. S., Carver, G., Chen, G., Crawford, J. H., Domine,
1091 F., Frey, M. M., Guzman, M. I., Heard, D. E., Helmig, D., Hoffmann, M. R.,
1092 Honrath, R. E., Huey, L. G., Hutterli, M., Jacobi, H. W., Klan, P., Lefer, B.,
1093 McConnell, J., Plane, J., Sander, R., Savarino, J., Shepson, P. B., Simpson, W. R.,
1094 Sodeau, J. R., von Glasow, R., Weller, R., Wolff, E. W., and Zhu, T.: An overview
1095 of snow photochemistry: evidence, mechanisms and impacts, *Atmos. Chem. Phys.*,
1096 7, 4329-4373, 10.5194/acp-7-4329-2007, 2007.

1097 Grannas, A. M., Pagano, L. P., Pierce, B. C., Bobby, R., and Fede, A.: Role of dissolved
1098 organic matter in ice photochemistry, *Environ. Sci. Technol.*, 48, 10725-10733,
1099 10.1021/es5023834, 2014.

1100 Hadley, O. L., and Kirchstetter, T. W.: Black-carbon reduction of snow albedo, *Nat.*
1101 *Clim. Chang.*, 2, 437-440, 10.1038/Nclimate1433, 2012.

1102 Hagler, G. S. W., Bergin, M. H., Smith, E. A., and Dibb, J. E.: A summer time series of
1103 particulate carbon in the air and snow at Summit, Greenland, *J. Geophys. Res.*
1104 *Atmos.*, 112, D21309, 10.1029/2007jd008993, 2007a.

1105 Hagler, G. S. W., Bergin, M. H., Smith, E. A., Dibb, J. E., Anderson, C., and Steig, E.
1106 J.: Particulate and water-soluble carbon measured in recent snow at Summit,
1107 Greenland, *Geophys. Res. Lett.*, 34, 10.1029/2007GL030110, 2007b.

1108 Hall, D. K., Riggs, G. A., and Salomonson, V. V.: Development of Methods for Mapping
1109 Global Snow Cover Using Moderate Resolution Imaging Spectroradiometer Data,
1110 *Remote Sens. Environ.*, 54, 127-140, 10.1016/0034-4257(95)00137-P, 1995.

1111 Handley, S. R., Clifford, D., and Donaldson, D. J.: Photochemical Loss of Nitric Acid
1112 on Organic Films: a Possible Recycling Mechanism for NO_x, *Environ. Sci.*
1113 *Technol.*, 41, 3898-3903, 10.1021/es062044z, 2007.

1114 Hansen, J., and Nazarenko, L.: Soot climate forcing via snow and ice albedos, *Proc.*
1115 *Nat. Acad. Sci. U.S.A.*, 101, 423-428, 10.1073/pnas.2237157100, 2004.

1116 He, C. L., Li, Q. B., Liou, K. N., Takano, Y., Gu, Y., Qi, L., Mao, Y. H., and Leung, L.
1117 R.: Black carbon radiative forcing over the Tibetan Plateau, *Geophys. Res. Lett.*,
1118 41, 7806-7813, 10.1002/2014GL062191, 2014.

1119 He, Z., Mao, J., Honeycutt, C. W., Ohno, T., Hunt, J. F., and Cade-Menun, B. J.:
1120 Characterization of plant-derived water extractable organic matter by multiple
1121 spectroscopic techniques, *Biol. Fert. Soils*, 45, 609-616, 10.1007/s00374-009-
1122 0369-8, 2009.

1123 Hertkorn, N., Benner, R., Frommberger, M., Schmitt-Kopplin, P., Witt, M., Kaiser, K.,
1124 Kettrup, A., and Hedges, J. I.: Characterization of a major refractory component
1125 of marine dissolved organic matter, *Geochim. Cosmochim. Acta*, 70, 2990-3010,
1126 10.1016/j.gca.2006.03.021, 2006.

1127 Hood, E., Fellman, J., Spencer, R. G. M., Hernes, P. J., Edwards, R., D'Amore, D., and
1128 Scott, D.: Glaciers as a source of ancient and labile organic matter to the marine
1129 environment, *Nature*, 462, 1044-1047, 10.1038/nature08580, 2009.

1130 Hood, E., Battin, T. J., Fellman, J., O'Neel, S., and Spencer, R. G. M.: Storage and
1131 release of organic carbon from glaciers and ice sheets, *Nat. Geosci.*, 8, 91-96,
1132 10.1038/NNGEO2331, 2015.

1133 Huang, J. P., Fu, Q. A., Zhang, W., Wang, X., Zhang, R. D., Ye, H., and Warren, S. G.:

1134 Dust And Black Carbon In Seasonal Snow across Northern China, *Bull. Am.*
1135 *Meteorol. Soc.*, 92, 175-181, 10.1175/2010BAMS3064.1, 2011.

1136 Hullar, T., Bononi, F. C., Chen, Z., Magadia, D., Palmer, O., Tran, T., Rocca, D.,
1137 Andreussi, O., Donadio, D., and Anastasio, C.: Photodecay of guaiacol is faster in
1138 ice, and even more rapid on ice, than in aqueous solution, *Environ. Sci.-Proc. Imp.*,
1139 22, 1666-1677, 10.1039/d0em00242a, 2020.

1140 Hunt, J. F., and Ohno, T.: Characterization of Fresh and Decomposed Dissolved Organic
1141 Matter Using Excitation–Emission Matrix Fluorescence Spectroscopy and
1142 Multiway Analysis, *J. Agric. Food. Chem.*, 55, 2121-2128, 10.1021/jf063336m,
1143 2007.

1144 Ikeya, K., Sleighter, R. L., Hatcher, P. G., and Watanabe, A.: Characterization of the
1145 chemical composition of soil humic acids using Fourier transform ion cyclotron
1146 resonance mass spectrometry, *Geochim. Cosmochim. Acta*, 153, 169-182,
1147 10.1016/j.gca.2015.01.002, 2015.

1148 Jacobson, M. Z.: Climate response of fossil fuel and biofuel soot, accounting for soot's
1149 feedback to snow and sea ice albedo and emissivity, *J. Geophys. Res. Atmos.*, 109,
1150 D21201, 10.1029/2004jd004945, 2004.

1151 Jaffé, R., Cawley, K. M., and Yamashita, Y.: Applications of Excitation Emission Matrix
1152 Fluorescence with Parallel Factor Analysis (EEM-PARAFAC) in Assessing
1153 Environmental Dynamics of Natural Dissolved Organic Matter (DOM) in Aquatic
1154 Environments: A Review, in: *Advances in the Physicochemical Characterization
1155 of Dissolved Organic Matter: Impact on Natural and Engineered Systems*, ACS
1156 Symposium Series, 1160, American Chemical Society, 27-73, 2014.

1157 Jin, Z. H., Charlock, T. P., Rutledge, K., Stamnes, K., and Wang, Y. J.: Analytical
1158 solution of radiative transfer in the coupled atmosphere-ocean system with a rough
1159 surface, *Appl. Opt.*, 45, 7443-7455, 10.1364/AO.45.007443, 2006.

1160 Jones, H. G.: The ecology of snow-covered systems: a brief overview of nutrient
1161 cycling and life in the cold, *Hydrol. Processes*, 13, 2135-2147,
1162 10.1002/(SICI)1099-1085(199910)13:14/15<2135::AID-HYP862>3.0.CO;2-Y,
1163 1999.

1164 Kim, S., Kramer, R. W., and Hatcher, P. G.: Graphical method for analysis of ultrahigh-
1165 resolution broadband mass spectra of natural organic matter, the van Krevelen
1166 diagram, *Anal. Chem.*, 75, 5336-5344, 10.1021/ac034415p, 2003.

1167 Kirchstetter, T. W., Novakov, T., and Hobbs, P. V.: Evidence that the spectral
1168 dependence of light absorption by aerosols is affected by organic carbon, *J.*
1169 *Geophys. Res. Atmos.*, 109, D21208, 10.1029/2004jd004999, 2004.

1170 Kirillova, E. N., Andersson, A., Han, J., Lee, M., and Gustafsson, O.: Sources and light
1171 absorption of water-soluble organic carbon aerosols in the outflow from northern
1172 China, *Atmos. Chem. Phys.*, 14, 1413-1422, 10.5194/acp-14-1413-2014, 2014.

1173 Koch, B. P., and Dittmar, T.: From mass to structure: an aromaticity index for high-
1174 resolution mass data of natural organic matter, *Rapid Commun. Mass Spectrom.*,
1175 20, 926-932, 10.1002/rcm.2386, 2006.

1176 Koch, B. P., and Dittmar, T.: From mass to structure: an aromaticity index for high-
1177 resolution mass data of natural organic matter, *Rapid Commun. Mass Spectrom.*,
1178 30, 250-250, 10.1002/rcm.7433, 2016.

1179 Kothawala, D. N., Murphy, K. R., Stedmon, C. A., Weyhenmeyer, G. A., and Tranvik,
1180 L. J.: Inner filter correction of dissolved organic matter fluorescence, *Limnol.*
1181 *Oceanogr.-Meth.*, 11, 616-630, 10.4319/Iom.2013.11.616, 2013.

1182 Kroll, J. H., Donahue, N. M., Jimenez, J. L., Kessler, S. H., Canagaratna, M. R., Wilson,
1183 K. R., Altieri, K. E., Mazzoleni, L. R., Wozniak, A. S., Bluhm, H., Mysak, E. R.,

1184 Smith, J. D., Kolb, C. E., and Worsnop, D. R.: Carbon oxidation state as a metric
1185 for describing the chemistry of atmospheric organic aerosol, *Nat. Chem.*, 3, 133-
1186 139, 10.1038/nchem.948, 2011.

1187 Laskin, A., Smith, J. S., Laskin, J. J. E. s., and technology: Molecular characterization
1188 of nitrogen-containing organic compounds in biomass burning aerosols using
1189 high-resolution mass spectrometry, *Environ. Sci. Technol.*, 43, 3764-3771,
1190 10.1021/es803456n, 2009.

1191 Laskin, A., Laskin, J., and Nizkorodov, S. A.: Chemistry of Atmospheric Brown Carbon,
1192 *Chem. Rev.*, 115, 4335-4382, 10.1021/cr5006167, 2015.

1193 Lawaetz, A. J., and Stedmon, C. A.: Fluorescence Intensity Calibration Using the
1194 Raman Scatter Peak of Water, *Appl. Spectrosc.*, 63, 936-940,
1195 10.1366/000370209788964548, 2009.

1196 Legrand, M., Preunkert, S., Jourdain, B., Guilhermet, J., Fain, X., Alekhina, I., and Petit,
1197 J. R.: Water-soluble organic carbon in snow and ice deposited at Alpine, Greenland,
1198 and Antarctic sites: a critical review of available data and their atmospheric
1199 relevance, *Clim. Past*, 9, 2195-2211, 10.5194/cp-9-2195-2013, 2013.

1200 Lin, P., Engling, G., and Yu, J. Z.: Humic-like substances in fresh emissions of rice
1201 straw burning and in ambient aerosols in the Pearl River Delta Region, China,
1202 *Atmos. Chem. Phys.*, 10, 6487-6500, 10.5194/acp-10-6487-2010, 2010.

1203 Lin, P., Rincon, A. G., Kalberer, M., and Yu, J. Z.: Elemental composition of HULIS in
1204 the Pearl River Delta Region, China: results inferred from positive and negative
1205 electrospray high resolution mass spectrometric data, *Environ. Sci. Technol.*, 46,
1206 7454-7462, 10.1021/es300285d, 2012.

1207 Lin, P., Aiona, P. K., Li, Y., Shiraiwa, M., Laskin, J., Nizkorodov, S. A., and Laskin, A.:
1208 Molecular Characterization of Brown Carbon in Biomass Burning Aerosol
1209 Particles, *Environ. Sci. Technol.*, 50, 11815-11824, 10.1021/acs.est.6b03024, 2016.

1210 Lin, P., Fleming, L. T., Nizkorodov, S. A., Laskin, J., and Laskin, A.: Comprehensive
1211 Molecular Characterization of Atmospheric Brown Carbon by High Resolution
1212 Mass Spectrometry with Electrospray and Atmospheric Pressure Photoionization,
1213 *Anal. Chem.*, 90, 12493-12502, 10.1021/acs.analchem.8b02177, 2018.

1214 Liu, Y. Q., Yao, T. D., Jiao, N. Z., Kang, S. C., Xu, B. Q., Zeng, Y. H., Huang, S. J., and
1215 Liu, X. B.: Bacterial diversity in the snow over Tibetan Plateau Glaciers,
1216 *Extremophiles*, 13, 411-423, 10.1007/s00792-009-0227-5, 2009.

1217 Lobodin, V. V., Marshall, A. G., and Hsu, C. S.: Compositional Space Boundaries for
1218 Organic Compounds, *Anal. Chem.*, 84, 3410-3416, 10.1021/ac300244f, 2012.

1219 Lu, Y., Li, X., Mesfioui, R., Bauer, J. E., Chambers, R. M., Canuel, E. A., and Hatcher,
1220 P. G.: Use of ESI-FTICR-MS to Characterize Dissolved Organic Matter in
1221 Headwater Streams Draining Forest-Dominated and Pasture-Dominated
1222 Watersheds, *Plos One*, 10, e0145639, 10.1371/journal.pone.0145639, 2015a.

1223 Lu, Z., Streets, D. G., Winijkul, E., Yan, F., Chen, Y., Bond, T. C., Feng, Y., Dubey, M.
1224 K., Liu, S., Pinto, J. P., and Carmichael, G. R.: Light absorption properties and
1225 radiative effects of primary organic aerosol emissions, *Environ. Sci. Technol.*, 49,
1226 4868-4877, 10.1021/acs.est.5b00211, 2015b.

1227 Lutz, S., Anesio, A. M., Villar, S. E. J., and Benning, L. G.: Variations of algal
1228 communities cause darkening of a Greenland glacier, *FEMS Microbiol. Ecol.*, 89,
1229 402-414, 10.1111/1574-6941.12351, 2014.

1230 McLafferty, F. W., Tureček, F., and Turecek, F.: Interpretation of mass spectra,
1231 University science books, 1993.

1232 McNeill, V. F., Grannas, A. M., Abbatt, J. P. D., Ammann, M., Ariya, P., Bartels-Rausch,
1233 T., Domine, F., Donaldson, D. J., Guzman, M. I., Heger, D., Kahan, T. F., Klan, P.,

1234 Masclin, S., Toubin, C., and Voisin, D.: Organics in environmental ices: sources,
1235 chemistry, and impacts, *Atmos. Chem. Phys.*, 12, 9653-9678, 10.5194/acp-12-
1236 9653-2012, 2012.

1237 Mead, R. N., Felix, J. D., Avery, G. B., Kieber, R. J., Willey, J. D., and Podgorski, D.
1238 C.: Characterization of CHOS compounds in rainwater from continental and
1239 coastal storms by ultrahigh resolution mass spectrometry, *Atmos. Environ.*, 105,
1240 162-168, 10.1016/j.atmosenv.2015.01.057, 2015.

1241 Mladenov, N., Alados-Arboledas, L., Olmo, F. J., Lyamani, H., Delgado, A., Molina,
1242 A., and Reche, I.: Applications of optical spectroscopy and stable isotope analyses
1243 to organic aerosol source discrimination in an urban area, *Atmos. Environ.*, 45,
1244 1960-1969, 10.1016/j.atmosenv.2011.01.029, 2011.

1245 Mladenov, N., Williams, M. W., Schmidt, S. K., and Cawley, K.: Atmospheric
1246 deposition as a source of carbon and nutrients to an alpine catchment of the
1247 Colorado Rocky Mountains, *Biogeosciences*, 9, 3337-3355, 10.5194/bg-9-3337-
1248 2012, 2012.

1249 Murphy, K. R., Stedmon, C. A., Waite, T. D., and Ruiz, G. M.: Distinguishing between
1250 terrestrial and autochthonous organic matter sources in marine environments using
1251 fluorescence spectroscopy, *Mar. Chem.*, 108, 40-58,
1252 10.1016/j.marchem.2007.10.003, 2008.

1253 Murphy, K. R., Stedmon, C. A., Graeber, D., and Bro, R.: Fluorescence spectroscopy
1254 and multi-way techniques. PARAFAC, *Anal. Methods*, 5, 6557-6566,
1255 10.1039/c3ay41160e, 2013.

1256 Myers, O. D., Sumner, S. J., Li, S., Barnes, S., and Du, X.: One Step Forward for
1257 Reducing False Positive and False Negative Compound Identifications from Mass
1258 Spectrometry Metabolomics Data: New Algorithms for Constructing Extracted
1259 Ion Chromatograms and Detecting Chromatographic Peaks, *Anal. Chem.*, 89,
1260 8696-8703, 10.1021/acs.analchem.7b00947, 2017.

1261 Ning, C., Gao, Y., Zhang, H., Yu, H., Wang, L., Geng, N., Cao, R., and Chen, J.:
1262 Molecular characterization of dissolved organic matters in winter atmospheric fine
1263 particulate matters (PM_{2.5}) from a coastal city of northeast China, *Sci. Total
1264 Environ.*, 689, 312-321, 10.1016/j.scitotenv.2019.06.418, 2019.

1265 Niu, H. W., Kang, S. C., Lu, X. X., and Shi, X. F.: Distributions and light absorption
1266 property of water soluble organic carbon in a typical temperate glacier,
1267 southeastern Tibetan Plateau, *Tellus B*, 70, 10.1080/16000889.2018.1468705,
1268 2018.

1269 Nizkorodov, S. A., Laskin, J., and Laskin, A.: Molecular chemistry of organic aerosols
1270 through the application of high resolution mass spectrometry, *Phys. Chem. Chem.
1271 Phys.*, 13, 3612-3629, 10.1039/c0cp02032j, 2011.

1272 Noziere, B., Kalberer, M., Claeys, M., Allan, J., D'Anna, B., Decesari, S., Finessi, E.,
1273 Glasius, M., Grgic, I., Hamilton, J. F., Hoffmann, T., Iinuma, Y., Jaoui, M., Kahnt,
1274 A., Kampf, C. J., Kourtev, I., Maenhaut, W., Marsden, N., Saarikoski, S.,
1275 Schnelle-Kreis, J., Surratt, J. D., Szidat, S., Szmigielski, R., and Wisthaler, A.: The
1276 molecular identification of organic compounds in the atmosphere: state of the art
1277 and challenges, *Chem. Rev.*, 115, 3919-3983, 10.1021/cr5003485, 2015.

1278 Ohno, T., He, Z., Sleighter, R. L., Honeycutt, C. W., and Hatcher, P. G.: Ultrahigh
1279 resolution mass spectrometry and indicator species analysis to identify marker
1280 components of soil- and plant biomass- derived organic matter fractions, *Environ.
1281 Sci. Technol.*, 44, 8594-8600, 10.1021/es101089t, 2010.

1282 Painter, T. H., Deems, J. S., Belnap, J., Hamlet, A. F., Landry, C. C., and Udall, B.:
1283 Response of Colorado River runoff to dust radiative forcing in snow, *Proc. Nat.*

1284 Acad. Sci. U.S.A., 107, 17125-17130, 10.1073/pnas.0913139107, 2010.

1285 Painter, T. H., Seidel, F. C., Bryant, A. C., McKenzie Skiles, S., and Rittger, K.: Imaging
1286 spectroscopy of albedo and radiative forcing by light-absorbing impurities in
1287 mountain snow, *J. Geophys. Res. Atmos.*, 118, 9511-9523, 10.1002/jgrd.50520,
1288 2013.

1289 Pluskal, T., Castillo, S., Villar-Briones, A., and Orešič, M.: MZmine 2: modular
1290 framework for processing, visualizing, and analyzing mass spectrometry-based
1291 molecular profile data, *BMC Bioinf.*, 11, 395, 10.1186/1471-2105-11-395, 2010.

1292 Pöhlker, C., Huffman, J. A., and Pöschl, U.: Autofluorescence of atmospheric
1293 bioaerosols – fluorescent biomolecules and potential interferences, *Atmos. Meas.*
1294 *Tech.*, 5, 37-71, 10.5194/amt-5-37-2012, 2012.

1295 Pu, W., Wang, X., Wei, H. L., Zhou, Y., Shi, J. S., Hu, Z. Y., Jin, H. C., and Chen, Q. L.:
1296 Properties of black carbon and other insoluble light-absorbing particles in seasonal
1297 snow of northwestern China, *The Cryosphere*, 11, 1213-1233, 10.5194/tc-11-
1298 1213-2017, 2017.

1299 Pu, W., Cui, J., Shi, T., Zhang, X., He, C., and Wang, X.: The remote sensing of radiative
1300 forcing by light-absorbing particles (LAPs) in seasonal snow over northeastern
1301 China, *Atmos. Chem. Phys.*, 19, 9949-9968, 10.5194/acp-19-9949-2019, 2019.

1302 Qi, Y., Fu, P., and Volmer, D. A.: Analysis of natural organic matter via fourier transform
1303 ion cyclotron resonance mass spectrometry: an overview of recent non-petroleum
1304 applications, *Mass Spectrom. Rev.*, 00, 1-15, 10.1002/mas.21634, 2020.

1305 Qian, Y., Wang, H., Zhang, R., Flanner, M. G., and Rasch, P. J.: A sensitivity study on
1306 modeling black carbon in snow and its radiative forcing over the Arctic and
1307 Northern China, *Environ. Res. Lett.*, 9, 10.1088/1748-9326/9/6/064001, 2014.

1308 Roach, P. J., Laskin, J., and Laskin, A.: Higher-order mass defect analysis for mass
1309 spectra of complex organic mixtures, *Anal. Chem.*, 83, 4924-4929,
1310 10.1021/ac200654j, 2011.

1311 Saleh, R.: From Measurements to Models: Toward Accurate Representation of Brown
1312 Carbon in Climate Calculations, *Curr. Pollut. Rep.*, 6, 90-104, 10.1007/s40726-
1313 020-00139-3, 2020.

1314 Seinfeld, J. H., and Pandis, S. N.: Atmospheric chemistry and physics: from air
1315 pollution to climate change, 3rd ed., John Wiley & Sons, 2016.

1316 Shi, T., Pu, W., Zhou, Y., Cui, J., Zhang, D., and Wang, X.: Albedo of Black Carbon-
1317 Contaminated Snow Across Northwestern China and the Validation With Model
1318 Simulation, *J. Geophys. Res. Atmos.*, 125, 10.1029/2019jd032065, 2020.

1319 Shick, J. M., and Dunlap, W. C.: Mycosporine-like amino acids and related Gadusols:
1320 biosynthesis, accumulation, and UV-protective functions in aquatic organisms,
1321 *Annu. Rev. Physiol.*, 64, 223-262, 10.1146/annurev.physiol.64.081501.155802,
1322 2002.

1323 Siegmann, K., and Sattler, K.: Formation mechanism for polycyclic aromatic
1324 hydrocarbons in methane flames, *J. Chem. Phys.*, 112, 698-709, 10.1063/1.480648,
1325 2000.

1326 Singer, G. A., Fasching, C., Wilhelm, L., Niggemann, J., Steier, P., Dittmar, T., and
1327 Battin, T. J.: Biogeochemically diverse organic matter in Alpine glaciers and its
1328 downstream fate, *Nat. Geosci.*, 5, 710-714, 10.1038/NGEO1581, 2012.

1329 Skiles, S. M., Flanner, M., Cook, J. M., Dumont, M., and Painter, T. H.: Radiative
1330 forcing by light-absorbing particles in snow, *Nat. Clim. Chang.*, 8, 964-971,
1331 10.1038/s41558-018-0296-5, 2018.

1332 Spencer, R. G. M., Guo, W. D., Raymond, P. A., Dittmar, T., Hood, E., Fellman, J., and
1333 Stubbins, A.: Source and biolability of ancient dissolved organic matter in glacier

1334 and lake ecosystems on the Tibetan Plateau, *Geochim. Cosmochim. Acta*, 142, 64-
1335 74, 10.1016/j.gca.2014.08.006, 2014.

1336 Stedmon, C. A., Markager, S., and Bro, R.: Tracing dissolved organic matter in aquatic
1337 environments using a new approach to fluorescence spectroscopy, *Mar. Chem.*, 82,
1338 239-254, 10.1016/S0304-4203(03)00072-0, 2003.

1339 Stedmon, C. A., and Markager, S.: Resolving the variability in dissolved organic matter
1340 fluorescence in a temperate estuary and its catchment using PARAFAC analysis,
1341 *Limnol. Oceanogr.*, 50, 686-697, 10.4319/lo.2005.50.2.0686, 2005.

1342 Stedmon, C. A., and Bro, R.: Characterizing dissolved organic matter fluorescence with
1343 parallel factor analysis: a tutorial, *Limnol. Oceanogr.-Meth.*, 6, 572-579,
1344 10.4319/lom.2008.6.572, 2008.

1345 Sun, H. L., Biedermann, L., and Bond, T. C.: Color of brown carbon: A model for
1346 ultraviolet and visible light absorption by organic carbon aerosol, *Geophys. Res.
1347 Lett.*, 34, L17813, 10.1029/2007gl029797, 2007.

1348 Toon, O. B., McKay, C. P., Ackerman, T. P., and Santhanam, K.: Rapid Calculation of
1349 Radiative Heating Rates and Photodissociation Rates in Inhomogeneous Multiple-
1350 Scattering Atmospheres, *J. Geophys. Res. Atmos.*, 94, 16287-16301,
1351 10.1029/JD094iD13p16287, 1989.

1352 Voisin, D., Jaffrezo, J. L., Houdier, S., Barret, M., Cozic, J., King, M. D., France, J. L.,
1353 Reay, H. J., Grannas, A., Kos, G., Ariya, P. A., Beine, H. J., and Domine, F.:
1354 Carbonaceous species and humic like substances (HULIS) in Arctic snowpack
1355 during OASIS field campaign in Barrow, *J. Geophys. Res. Atmos.*, 117, D00r19,
1356 10.1029/2011jd016612, 2012.

1357 Wang, K., Zhang, Y., Huang, R.-J., Cao, J., and Hoffmann, T.: UHPLC-Orbitrap mass
1358 spectrometric characterization of organic aerosol from a central European city
1359 (Mainz, Germany) and a Chinese megacity (Beijing), *Atmos. Environ.*, 189, 22-
1360 29, 10.1016/j.atmosenv.2018.06.036, 2018.

1361 Wang, X., Doherty, S. J., and Huang, J.: Black carbon and other light-absorbing
1362 impurities in snow across Northern China, *J. Geophys. Res. Atmos.*, 118, 1471-
1363 1492, 10.1029/2012JD018291, 2013.

1364 Wang, X., Hayeck, N., Brüggemann, M., Yao, L., Chen, H., Zhang, C., Emmelin, C.,
1365 Chen, J., George, C., and Wang, L.: Chemical Characteristics of Organic Aerosols
1366 in Shanghai: A Study by Ultrahigh-Performance Liquid Chromatography Coupled
1367 With Orbitrap Mass Spectrometry, *J. Geophys. Res. Atmos.*, 122, 11,703-711,722,
1368 10.1002/2017jd026930, 2017a.

1369 Wang, X., Pu, W., Ren, Y., Zhang, X., Zhang, X., Shi, J., Jin, H., Dai, M., and Chen, Q.:
1370 Observations and model simulations of snow albedo reduction in seasonal snow
1371 due to insoluble light-absorbing particles during 2014 Chinese survey, *Atmos.
1372 Chem. Phys.*, 17, 2279-2296, 10.5194/acp-17-2279-2017, 2017b.

1373 Wang, X., Hayeck, N., Brüggemann, M., Abis, L., Riva, M., Lu, Y., Wang, B., Chen, J.,
1374 George, C., and Wang, L.: Chemical characteristics and brown carbon
1375 chromophores of atmospheric organic aerosols over the Yangtze River channel: a
1376 cruise campaign, *J. Geophys. Res. Atmos.*, 10.1029/2020jd032497, 2020a.

1377 Wang, X., Zhang, X., and Di, W.: Development of an improved two-sphere integration
1378 technique for quantifying black carbon concentrations in the atmosphere and
1379 seasonal snow, *Atmos. Meas. Tech.*, 13, 39-52, 10.5194/amt-13-39-2020, 2020b.

1380 Wiscombe, W. J., and Warren, S. G.: A Model for the Spectral Albedo of Snow .1. Pure
1381 Snow, *J. Atmos. Sci.*, 37, 2712-2733, 10.1175/1520-
1382 0469(1980)037<2712:AMFTSA>2.0.CO;2, 1980.

1383 Wu, C., Yang, J., Fu, Q., Zhu, B., Ruan, T., and Jiang, G.: Molecular characterization

1384 of water-soluble organic compounds in PM_{2.5} using ultrahigh resolution mass
1385 spectrometry, *Sci. Total Environ.*, 668, 917-924, 10.1016/j.scitotenv.2019.03.031,
1386 2019a.

1387 Wu, G., Ram, K., Fu, P., Wang, W., Zhang, Y., Liu, X., Stone, E. A., Pradhan, B. B.,
1388 Dangol, P. M., Panday, A. K., Wan, X., Bai, Z., Kang, S., Zhang, Q., and Cong, Z.:
1389 Water-Soluble Brown Carbon in Atmospheric Aerosols from Godavari (Nepal), a
1390 Regional Representative of South Asia, *Environ. Sci. Technol.*, 53, 3471-3479,
1391 10.1021/acs.est.9b00596, 2019b.

1392 Wu, G., Wan, X., Ram, K., Li, P., Liu, B., Yin, Y., Fu, P., Loewen, M., Gao, S., Kang,
1393 S., Kawamura, K., Wang, Y., and Cong, Z.: Light absorption, fluorescence
1394 properties and sources of brown carbon aerosols in the Southeast Tibetan Plateau,
1395 *Environ. Pollut.*, 257, 113616, 10.1016/j.envpol.2019.113616, 2020.

1396 Wu, G., Fu, P., Ram, K., Song, J., Chen, Q., Kawamura, K., Wan, X., Kang, S., Wang,
1397 X., Laskin, A., and Cong, Z.: Fluorescence characteristics of water-soluble organic
1398 carbon in atmospheric aerosol, *Environ. Pollut.*, 268, 115906,
1399 <https://doi.org/10.1016/j.envpol.2020.115906>, 2021.

1400 Xie, Q., Su, S., Chen, S., Zhang, Q., Yue, S., Zhao, W., Du, H., Ren, H., Wei, L., dong,
1401 c., Xu, Y.-s., Sun, Y., Wang, Z., and Fu, P.: Molecular Characterization of Size-
1402 Segregated Organic Aerosols in the Urban Boundary Layer in Wintertime Beijing
1403 by FT-ICR MS, *Faraday Discuss.*, 10.1039/d0fd00084a, 2020.

1404 Xu, C., Chen, Y., Yang, Y., Hao, X., and Shen, Y.: Hydrology and water resources
1405 variation and its response to regional climate change in Xinjiang, *J. Geog. Sci.*, 20,
1406 599-612, 10.1007/s11442-010-0599-6, 2010.

1407 Yan, F. P., Kang, S. C., Li, C. L., Zhang, Y. L., Qin, X., Li, Y., Zhang, X. P., Hu, Z. F.,
1408 Chen, P. F., Li, X. F., Qu, B., and Sillanpää, M.: Concentration, sources and light
1409 absorption characteristics of dissolved organic carbon on a medium-sized valley
1410 glacier, northern Tibetan Plateau, *Cryosphere*, 10, 2611-2621, 10.5194/tc-10-
1411 2611-2016, 2016.

1412 Yang, W., Han, C., Yang, H., and Xue, X.: Significant HONO formation by the
1413 photolysis of nitrates in the presence of humic acids, *Environ. Pollut.*, 243, 679-
1414 686, 10.1016/j.envpol.2018.09.039, 2018.

1415 Ye, H., Zhang, R. D., Shi, J. S., Huang, J. P., Warren, S. G., and Fu, Q.: Black carbon
1416 in seasonal snow across northern Xinjiang in northwestern China, *Environ. Res.*
1417 *Lett.*, 7, 044002, 10.1088/1748-9326/7/4/044002, 2012.

1418 Zatzko, M. C., Grenfell, T. C., Alexander, B., Doherty, S. J., Thomas, J. L., and Yang, X.:
1419 The influence of snow grain size and impurities on the vertical profiles of actinic
1420 flux and associated NO_x emissions on the Antarctic and Greenland ice sheets,
1421 *Atmos. Chem. Phys.*, 13, 3547-3567, 2013.

1422 Zhang, Y., Kang, S., Gao, T., Schmale, J., Liu, Y., Zhang, W., Guo, J., Du, W., Hu, Z.,
1423 Cui, X., and Sillanpää, M.: Dissolved organic carbon in snow cover of the Chinese
1424 Altai Mountains, Central Asia: Concentrations, sources and light-absorption
1425 properties, *Sci. Total Environ.*, 647, 1385-1397, 10.1016/j.scitotenv.2018.07.417,
1426 2019.

1427 Zhang, Y., Kang, S., Gao, T., Sprenger, M., Dou, T., Han, W., Zhang, Q., Sun, S., Du,
1428 W., Chen, P., Guo, J., Cui, X., and Sillanpää, M.: Dissolved organic carbon in
1429 Alaskan Arctic snow: concentrations, light-absorption properties, and
1430 bioavailability, *Tellus B*, 72, 1-19, 10.1080/16000889.2020.1778968, 2020.

1431 Zhang, Y. L., Zhang, E. L., Yin, Y., van Dijk, M. A., Feng, L. Q., Shi, Z. Q., Liu, M. L.,
1432 and Qin, B. Q.: Characteristics and sources of chromophoric dissolved organic
1433 matter in lakes of the Yungui Plateau, China, differing in trophic state and altitude,

1434 Limnol. Oceanogr., 55, 2645-2659, 10.4319/lo.2010.55.6.2645, 2010.

1435 Zhang, Y. L., El-Haddad, I., Huang, R. J., Ho, K. F., Cao, J. J., Han, Y. M., Zotter, P.,
 1436 Bozzetti, C., Daellenbach, K. R., Slowik, J. G., Salazar, G., Prevot, A. S. H., and
 1437 Szidat, S.: Large contribution of fossil fuel derived secondary organic carbon to
 1438 water soluble organic aerosols in winter haze in China, *Atmos. Chem. Phys.*, 18,
 1439 4005-4017, 10.5194/acp-18-4005-2018, 2018a.

1440 Zhang, Y. L., Kang, S. C., Sprenger, M., Cong, Z. Y., Gao, T. G., Li, C. L., Tao, S., Li,
 1441 X. F., Zhong, X. Y., Xu, M., Meng, W. J., Neupane, B., Qin, X., and Sillanpaa, M.:
 1442 Black carbon and mineral dust in snow cover on the Tibetan Plateau, *The
 1443 Cryosphere*, 12, 413-431, 10.5194/tc-12-413-2018, 2018b.

1444 Zhao, C., Hu, Z., Qian, Y., Leung, L. R., Huang, J., Huang, M., Jin, J., Flanner, M. G.,
 1445 Zhang, R., Wang, H., Yan, H., Lu, Z., and Streets, D. G.: Simulating black carbon
 1446 and dust and their radiative forcing in seasonal snow: a case study over North
 1447 China with field campaign measurements, *Atmos. Chem. Phys.*, 14, 11475-11491,
 1448 10.5194/acp-14-11475-2014, 2014.

1449 Zhao, Y., Song, K., Wen, Z., Li, L., Zang, S., Shao, T., Li, S., and Du, J.: Seasonal
 1450 characterization of CDOM for lakes in semiarid regions of Northeast China using
 1451 excitation–emission matrix fluorescence and parallel factor analysis (EEM–
 1452 PARAFAC), *Biogeosciences*, 13, 1635-1645, 10.5194/bg-13-1635-2016, 2016.

1453 Zhou, L., Zhou, Y., Hu, Y., Cai, J., Liu, X., Bai, C., Tang, X., Zhang, Y., Jang, K. S.,
 1454 Spencer, R. G. M., and Jeppesen, E.: Microbial production and consumption of
 1455 dissolved organic matter in glacial ecosystems on the Tibetan Plateau, *Water Res.*,
 1456 160, 18-28, 10.1016/j.watres.2019.05.048, 2019a.

1457 Zhou, Y., Wen, H., Liu, J., Pu, W., Chen, Q., and Wang, X.: The optical characteristics
 1458 and sources of chromophoric dissolved organic matter (CDOM) in seasonal snow
 1459 of northwestern China, *The Cryosphere*, 13, 157-175, 10.5194/tc-13-157-2019,
 1460 2019b.

1461 Zhou, Y., Zhou, L., He, X., Jang, K. S., Yao, X., Hu, Y., Zhang, Y., Li, X., Spencer, R.
 1462 G. M., Brookes, J. D., and Jeppesen, E.: Variability in Dissolved Organic Matter
 1463 Composition and Biolability across Gradients of Glacial Coverage and Distance
 1464 from Glacial Terminus on the Tibetan Plateau, *Environ. Sci. Technol.*, 53, 12207-
 1465 12217, 10.1021/acs.est.9b03348, 2019c.